Generated using version 3.2 of the official AMS LaTeX template

Optimization of a radiative transfer forward operator for simulating SMOS brightness temperatures over the Upper Mississippi Basin, USA

H. Lievens, * N. E. C. Verhoest, B. Martens and M. J. van den Berg

Laboratory of Hydrology and Water Management, Ghent University, Ghent, Belgium

A. Al Bitar, S. Kumar Tomer, O. Merlin, F. Cabot and Y. Kerr

Centre d'Etudes Spatiales de la Biosphère, Toulouse, France

G. J. M. De Lannoy

Global Modeling and Assimilation Office, NASA Goddard Space Flight Center, Greenbelt, MD, USA

M. Drusch

European Space Agency, Noordwijk, The Netherlands

H.-J. Hendricks-Franssen and H. Vereecken

Forschungszentrum Jülich, Jülich, Germany

M. Pan and E. F. Wood

Land Surface Hydrology Group, Princeton University, Princeton, NJ, USA

G. Dumedah, J. P. Walker and V. R. N. Pauwels

Department of Civil Engineering, Monash University, Victoria, Australia

ABSTRACT

The Soil Moisture and Ocean Salinity (SMOS) satellite mission is routinely providing global multi-angular observations of brightness temperature (TB) at both horizontal and vertical polarization with a 3-day repeat period. The assimilation of such data into a land surface model (LSM) may improve the skill of operational flood forecasts through an improved estimation of soil moisture (SM). To accommodate for the direct assimilation of the SMOS TB data, the LSM needs to be coupled with a radiative transfer model (RTM), serving as a forward operator for the simulation of multi-angular and multi-polarization top of atmosphere TBs. This study investigates the use of the Variable Infiltration Capacity (VIC) LSM coupled with the Community Microwave Emission Modelling platform (CMEM) for simulating SMOS TB observations over the Upper Mississippi basin, USA. For a period of 2 years (2010-2011), a comparison between SMOS TBs and simulations with literature-based RTM parameters reveals a basin averaged bias of 30 K. Therefore, time series of SMOS TB observations are used to investigate ways for mitigating these large biases. Specifically, the study demonstrates the impact of the LSM soil moisture climatology in the magnitude of TB biases. After CDF matching the SM climatology of the LSM to SMOS retrievals, the average bias decreases from 30 K to less than 5 K. Further improvements can be made through calibration of RTM parameters related to the modeling of surface roughness and vegetation. Consequently, it can be concluded that SM rescaling and RTM optimization are efficient means for mitigating biases and form a necessary preparatory step for data assimilation.

* *Corresponding author address:* Hans Lievens, Laboratory of Hydrology and Water Management, Ghent University, Coupure links 653, Ghent, Belgium.

E-mail: Hans.Lievens@UGent.be

1. Introduction

The updating of land surface models (LSMs) through remote sensing data assimilation is well-known for its potential to improve hydrologic model predictions (e.g. Pauwels et al. (2001, 2002); Crow and Wood (2003); Reichle et al. (2007); Pan et al. (2009)). Often, the LSMs are updated with observations of the top surface soil moisture (SM) content, since it plays a key role in the partitioning of rainfall into infiltration, runoff, and evapotranspiration. The updating of surface SM may substantially improve the profile SM along, since the errors in surface SM predictions are highly correlated with those at deeper depths (Walker et al. 2001).

The significance of SM observations for hydrologic predictions has fostered the development of remote sensing platforms, such as the Soil Moisture and Ocean Salinity (SMOS) mission (Kerr et al. 2001) and the Soil Moisture Active and Passive (SMAP) mission (Entekhabi et al. 2010), dedicated to observing the dynamics of SM across time and space. These radiometer systems provide indirect estimates of SM, through the close relationship between the observed brightness temperature (TB) emitted by the Earths surface and the SM content. While it is possible to assimilate the derived SM products, there has been a strong interest in the direct assimilation of satellite-observed TBs (Reichle et al. 2001; Balsamo et al. 2006; Han et al. 2013), since this bypasses the need for ancillary parameters (e.g. surface temperature), and allows for the use of consistent parameters (e.g. soil and vegetation) between the LSM and radiative transfer model (RTM).

The assimilation of TB observations directly requires the use of an RTM as a forward operator, to simulate the top of atmosphere (TOA) TB. However, simulation of unbiased and accurate TBs is far from straightforward due to the complexity of the radiative transfer processes involved (De Lannoy et al. 2013). Furthermore, the parameters in RTMs are typically estimated from local field experiments using ground-based and airborne radiometers (e.g. Sabater et al. (2011); Peischl et al. (2012)), which may not always be appropriate for the simulation of space-borne observations, e.g. by SMOS. Unfortunately, large scale studies on RTM parameterization are hardly available (Drusch et al. 2009; de Rosnay et al. 2009), and only few studies have used actual SMOS TB data (De Lannoy et al. 2013; Montzka et al. 2013). Another major difficulty in TB simulation relates to the representation of the RTM input fields, such as soil temperature, soil moisture, and vegetation parameters, which are generally obtained from an LSM. Many studies have found large systematic differences between SM fields modeled through LSMs and those observed by satellite missions (e.g. Reichle et al. (2004); Gao et al. (2006); Sahoo et al. (2013)). These can be attributed to several factors (Verhoest et al. 2014), such as approximations and shortcomings in both the retrieval and land surface models (De Lannoy et al. 2007), and a mismatch in the vertical representation (Wilker et al. 2006). Radiometer observations are generally sensitive to only the top few centimeters (Escorihuela et al. 2010), whereas each LSM typically has its own definition of the top surface layer which is often much thicker than this (Sahoo et al. 2013). Furthermore, there is often a mismatch in horizontal resolution. Especially for regional and smaller scale studies, LSMs typically operate at resolutions of 1 to 10 km, whilst radiometers provide SM at scales of 10 to 40 km (Sahoo et al. 2013). Finally, LSMs may be optimized toward the simulation of streamflow or land-atmosphere fluxes, rather than SM representation. For these reasons, LSMs and satellite retrievals generally have different SM climatologies. Unfortunately, an established consensus on the climatology of SM over large domains, considering both LSMs and satellite retrievals, is currently lacking (Draper et al. 2013). Nevertheless, when LSM soil moisture is used as input to an RTM, its climatology has a substantial impact on the magnitude of biases in TB. This becomes evident when considering the sensitivity of TB to SM, i.e. generally in the order of 2 to 3 K increase per $0.01\,\mathrm{m}^3\,\mathrm{m}^{-3}$ decrease in SM for low vegetation at around 40° incidence angle (Jackson 1993).

In this study, the Community Microwave Emission Modelling (CMEM) platform (Holmes et al. 2008; Drusch et al. 2009; de Rosnay et al. 2009) is coupled to the Variable Infiltration Capacity (VIC) LSM (Liang et al. 1994, 1996, 1999) for the simulation of multi-angular and multi-polarization SMOS TB observations. The TB simulations from this model configuration are matched to SMOS observations by calibrating the RTM parameters accordingly. Previous studies have addressed the global calibration of RTM parameters based on multi-angular SMOS observations (De Lannoy et al. 2013), and local calibration of temporally dynamic RTM parameters through data assimilation over a SCAN (Soil Climate Analysis Network) site in Colorado (Montzka et al. 2013). The novelty of this present study lies in its focus on the influence of the LSM soil moisture climatology on the TB simulations, the selection of the RTM calibration parameters, and the dependence of the calibration on the sensor configuration (— i.e. distinguishing between ascending (A) and descending (D) satellite overpasses and horizontal (H) and vertical (V) polarizations). The study is applied on a regional scale, covering the Upper Mississippi Basin in the central US. The final aim of this study is to improve the parameterization of an RTM within a framework that accommodates for the direct assimilation of multi-angular and multi-polarization TB observations into an LSM, in order to benefit surface water management.

2. Data and methods

a. Study site

The Upper Mississippi River Basin is located in central US. The basin covers an area of about 440000 km^2, and comprises portions of Minnesota, Wisconsin, Iowa and Illinois. As can be seen in Figure 1, the land use is primarily agricultural (e.g. corn, soybean, wheat, etc.), with forests occurring in the Northeast. The basin is characterized by a lack of significant topography, which facilitates the retrieval of SM from satellite observations. The annual precipitation ranges from approximately 475 mm in the North to over 1300 mm in the South. The southern portion is prone to flooding due to strong summer precipitation, often enhanced by wet initial conditions. Furthermore, the basin is equipped with an extensive meteorological network, and is a part of the North American Land Data Assimilation System (NLDAS) domain (Mitchell et al. 2004). Finally, the catchment is characterized by a low contamination of radio frequency interference (RFI) in the SMOS L-band observations.

b. SMOS observations

SMOS provides regular (±3-day repeat period) observations of the TOA TB at global scale, which are operationally used for SM retrieval through the ESA (European Space Agency) Level 2 processor (Kerr et al. 2012). The TB and SM data in this study stem from the Level 3 CATDS (Centre Aval de Traitement des Données SMOS) product (Jacquette et al. 2010). In essence, the Level 3 algorithm is an extension of the Level 2 prototype, employing multi-orbit retrievals of vegetation parameters for the enhancement of SM retrievals over individual orbits.

The Level 3 CATDS TB data is a global daily product in full polarization, available in ±25 km cylindrical projection over the EASE (Equal Area Scalable Earth) grid. Note that the actual resolution of SMOS is ±43 km. The TB data are transformed from antenna polarization reference (X and Y) to ground reference (H and V) frame, and are angle-binned into fixed angle classes, stretching from 17.5° to 52.5°, with 5° bins. Both ascending and descending data have been extracted over the Upper Mississippi Basin from begin January 2010 to end December 2011, with ascending and descending orbits being processed separately.

Corresponding Level 3 CATDS ascending and descending SM data are also extracted over the study area from 2010 to 2011 from the 1-day global product. Next to SM, the product also contains quality indices for soil moisture and RFI, as well as science flags indicating the presence of snow, frozen soils, etc. The SMOS data have been extensively filtered, preserving data when soil and air temperatures (according to the LSM forcings and simulations) are larger than 2.5°C, flags for snow and frozen soils (provided by the European Centre for Medium-Range Weather Forecasts) are zero, the probability of RFI is less than 0.2, and fractions of urban and water cover are less than 0.1 (fraction per SMOS cell).

c. *The Variable Infiltration Capacity model*

The Variable Infiltration Capacity (VIC) model (Liang et al. 1994, 1996, 1999) is a distributed LSM, conserving both the water and energy budgets. During the last decades, the VIC model has been widely-used in a number of applications (e.g. Maurer et al. (2001); Nijssen et al. (2001); Sheffield et al. (2003); Sheffield and Wood (2008)). The grid cell size of VIC can vary from 1 km to hundreds of kilometers, where each cell can be further subdivided into fractions representing specific vegetation types. In this study, the grid spacing corresponds to 0.125° by 0.125°.

The simulations make use of the real-time forcing dataset (Cosgrove et al. 2003) prepared for the first and second phase of the NLDAS project (Mitchell et al. 2004). Seven meteorological forcing fields were processed at an hourly time step and 0.125° spatial resolution: precipitation, 2-meter air temperature, pressure, vapor pressure, wind speed, and incoming shortwave and longwave radiation. The soil and vegetation parameters employed in VIC were sourced from the NLDAS-1 project, whereas land cover was extracted from the global 1-km University of Maryland (UMD) dataset (Hansen et al. 2000). The vegetation leaf area index (LAI) is based on the AVHRR (Advanced Very High Resolution Radiometer) satellite sensor (Gutman and Ignatov 1998). Finally, soil texture was derived from the State Soil Geographic (STATSGO) database (Miller and White 1998), whereas the elevation is described by the global 30 arc-second elevation (GTOPO30) database (Verdin and Greenlee 1996).

The model simulations over the Upper Mississippi are performed in full water and energy balance mode, where soil moisture and surface temperature in various layers are simulated on an hourly basis. The number of vertical soil layers has been set to 3, where the first layer represents the top 10 cm of the soil and the second and third layer depths vary between 10 cm and 250 cm. Note that this first layer depth may differ from the layer depth observed by SMOS, and may therefore contribute to the occurrence of SM bias between the model simulations and SMOS retrievals. Nevertheless, it was decided not to modify the first layer depth of VIC, as the model employs a one-source energy balance, and consequently depends on an equivalent surface and vegetation temperature. It should also be remarked that, for this study, the VIC model parameterization was considered to be fixed, having been previously optimized for the purpose of streamflow simulations (Maurer et al. 2002) over the Upper Mississippi Basin.

d. The Community Microwave Emission Modelling platform

The RTM coupled to VIC is the Community Microwave Emission Modelling (CMEM) platform (Holmes et al. 2008; Drusch et al. 2009; de Rosnay et al. 2009) version 4.1. CMEM is used as a forward operator to convert the simulated soil moisture and surface temperatures by VIC into simulations of multi-angular and multi-polarization TOA L-band brightness temperatures $\mathrm{TB}_{\mathrm{TOA},p}$ at polarization $p = [\mathrm{H}, \mathrm{V}]$:

$$\mathrm{TB}_{\mathrm{TOA},p} = \mathrm{TB}_{\mathrm{au},p} + \exp\left(-\tau_{\mathrm{atm},p}\right)\mathrm{TB}_{\mathrm{TOV},p}, \tag{1}$$

with $\mathrm{TB}_{\mathrm{au},p}$ [K] the upward atmospheric contribution, $\tau_{\mathrm{atm},p}$ $[-]$ the atmospheric opacity, and $\mathrm{TB}_{\mathrm{TOV},p}$ [K] the TB at top of vegetation (TOV). The latter is calculated through a first-order tau-omega ($\tau - \omega$) model:

$$\mathrm{TB}_{\mathrm{TOV},p} = \mathrm{T}_{\mathrm{eff}}\left(1 - r_p\right)\Gamma_p + \mathrm{T}_{\mathrm{c}}\left(1 - \omega_p\right)\left(1 - \Gamma_p\right)\left(1 + r_p\Gamma_p\right) + \mathrm{TB}_{\mathrm{ad},p} r_p \Gamma_p^2, \tag{2}$$

with $\mathrm{T}_{\mathrm{eff}}$ [K] the effective temperature of the soil medium, r_p $[-]$ the rough surface reflectivity, Γ_p $[-]$ the vegetation transmissivity, T_{c} [K] the canopy temperature (set equal to the surface temperature), ω_p $[-]$ the scattering albedo, and $\mathrm{TB}_{\mathrm{ad},p}$ [K] the downward atmospheric contribution. The transmissivity of the vegetation can be expressed by:

$$\Gamma_p = \exp\left(-\frac{\tau_{\mathrm{veg},p}}{\cos\theta}\right), \tag{3}$$

with $\tau_{\mathrm{veg},p}$ $[-]$ the optical depth of the standing vegetation and θ $[^\circ]$ the incidence angle.

CMEM has a modular structure, allowing for different parameterization options for the respective contributions from atmosphere, soil, and vegetation. In general, the options selected for this study revert to the L-MEB formulation by Wigneron et al. (2007). The atmospheric contributions ($TB_{au,p}$, $TB_{ad,p}$ and $\tau_{atm,p}$) are described according to Pellarin et al. (2003). For the soil component, the effective temperature T_{eff} is approximated based on the surface temperature T_{surf} [K] and the deep-soil temperature T_{deep} [K] as:

$$\mathrm{T_{eff}} = \mathrm{T_{deep}} + (\mathrm{T_{surf}} - \mathrm{T_{deep}})\, C, \tag{4}$$

where the weighting factor C depends on the SM content (Wigneron et al. 2001) by:

$$C = (\mathrm{SM}/w_0)^{b_{w_0}}, \tag{5}$$

with w_0 and b_{w_0} semi-empirical parameters depending on soil characteristics (mainly soil texture). As the RTM model is coupled with VIC, the first (0–10 cm) and third (variable thickness) layer VIC soil temperatures are used to approximate the T_{surf} and T_{deep}, whereas SM is approximated by the first layer SM from VIC.

The rough surface reflectivity parameterization is based on the Q/h formulation by Choudhury et al. (1979):

$$r_p = (QR_q + (1 - Q)\, R_p) \exp\left(-h \cos^{Nr_p}(\theta)\right), \tag{6}$$

with Q the polarization mixing factor often set to 0 for L-band (Wigneron et al. 2001), q the opposite polarization of p, h the surface roughness, Nr_p the angular dependence of the surface roughness, and R_p the smooth surface reflectivity. The latter is given by the Fresnel equations and is a function of the dielectric constant. The relationship between dielectric constant and soil moisture is described by Mironov et al. (2004). Finally, the vegetation optical depth is based on the model by Wigneron et al. (2007), which expresses $\tau_{veg,p}$ as a function of the optical depth at nadir τ_{NAD} [−]:

$$\tau_{\mathrm{veg},p} = \tau_{\mathrm{NAD}} \left(\cos^2(\theta) tt_p \sin^2(\theta)\right), \tag{7}$$

where tt_p is a parameter accounting for the influence of the incidence angle. The optical depth at nadir is given by:

$$\tau_{\mathrm{NAD}} = b_1 \mathrm{LAI} + b_2, \tag{8}$$

with b_1 and b_2 being structural vegetation parameters, and LAI the leaf area index.

A set of baseline parameter values has been identified, which correspond to the parameter values that are used in the ESA Level 2 processor v5.5.1 (Kerr et al. 2012). The list of parameters is given in Table 1 for each UMD land cover class. Note that for high vegetation types (classes 2 to 7 in Table 1), the annual maximum LAI is used in Equation 8, whereas for low vegetation types (classes 8 to 13 in Table 1), monthly average values (the same as in VIC) are employed.

3. CMEM optimization

In order to minimize climatological differences between the observed TBs from SMOS and the simulated TBs from the coupled model, a number of RTM parameters are calibrated using multi-angular and multi-polarization SMOS observations. The parameters that are considered for calibration are h, Nr_p, b_1, b_2, and τ_p, which were selected based on De Lannoy et al. (2013) and a sensitivity analysis. The b_1 and b_2 coefficients relate the optical thickness of the vegetation to LAI, the h and Nr_p parameters describe the surface roughness and its angular dependence, and τ_p controls the vegetation scattering of microwaves.

The following section outlines the calibration procedure and experiments. The calibration is based on SMOS observations and corresponding simulations for the year 2010, whereas data from the year 2011 are used for validation purposes. The calibration will be performed per UMD land cover class (Table 1), except for classes with cover fractions below 1% (such as grasslands), as these may be subject to less accurate parameterization due to under-representation in the calibration dataset. Also water and urban are not included, since the SMOS observations over cells dominated by the latter classes have been filtered.

a. Cal/Val data sets

For each SMOS Level 3 TB observation (including various angle bins and H/V-polarizations) in the 2010 calibration set, 25 EASE grid cells within the Upper Mississippi Basin are randomly selected (different grid cells are selected for each observation date). Note that a random selection of cells is performed to limit the size of the calibration data set, while including data from various locations within the basin. For each of the VIC cells that lay within the selected EASE grids (i.e. between 4 and 9 cells), the soil moisture (surface layer), soil temperatures (two layers), sand and clay fractions, and bulk density of VIC are used as input for CMEM. Also used are the VIC land cover types, fractions, and LAI for each VIC sub-grid vegetation layer. Next, CMEM is run for each individual VIC sub-grid vegetation fraction, for both H- and V-polarization and for 8 angle bins from 17.5° to 52.5° (each 5°). The simulated TBs are then aggregated to the VIC cell size according to the vegetation fractions within each cell. Finally, the SMOS antenna weight for each VIC grid cell is used to upscale the simulated TBs to the SMOS grid cell. Note that the antenna weighting differs for each cell, as it relies on the SMOS incidence angle, the azimuth angle, and the footprint axis. Thereby, the average of the mean value over each bin is used to compute the weighting function. By repeating the above mentioned steps for each multi-angular and multi-polarization SMOS observation, a calibration data set is established, which conserves the sub-grid vegetation description of the LSM, and comprises data from different incidence angles and polarizations, scattered over the study area. Hereby, independent calibration sets are generated for ascending and descending orbits, to investigate the impact of the overpass on the calibration performance. The same procedure is used for the generation of the validation data set based on data from 2011. The ascending and descending calibration and validation data sets each contain in total 8100 data points (TB observations at the SMOS grid) for each polarization. These comprise all 8 angle bins with a frequency of occurrence according to the spatial coverage of the angle bin over each of the randomly chosen cell locations. This implies that inner angles (e.g. 42.5°) are slightly more present than the outer angles (e.g. 17.5° and 52.5°) in the data sets used for calibration and validation.

It should be emphasized that the calibration of the RTM in this study is performed per land cover class instead of on a pixel basis. Pixel-based calibration is difficult to achieve if the goal is to preserve the sub-grid pixel heterogeneity in terms of vegetation types. Preserving sub-grid variability in a pixel based calibration would require a high number of parameter sets for each pixel, which would render the model coupling unfeasible.

b. Calibration algorithm

The calibration is performed using the Particle Swarm Optimization (PSO, Kennedy and Eberhart (1995)) algorithm. Example applications and details on PSO can be found in Scheerlinck et al. (2009); Pauwels and De Lannoy (2011). Only a brief explanation and summary of the selected PSO parameter values are given here. The PSO algorithm iteratively explores the parameter space and minimizes an a priori defined objective function. The PSO algorithm modifies a number of parameter sets (or particles) by changing their velocity (speed and direction) based on the most favorable conditions encountered by an individual particle and the swarm of particles. Thereby, the modification of individual particles expresses the cognitive aspect of the optimization algorithm, whereas the modification of the particle swarm accounts for the social aspect. In this study, the particle swarm size is set to 25, and the maximum number of iterations to 30. The inertia weight, cognitive and social parameters are respectively set to 0.7, 0.7, and 1.3. The selected PSO parameter values are based on De Lannoy et al. (2013), and enforce a stronger social than cognitive effect on the optimization.

The objective function J to be minimized integrates the Kling-Gupta-Efficiency (KGE), introduced by Gupta et al. (2009), together with a parameter penalty term as:

$$J = W_{\mathrm{KGE}} \frac{1}{N_{\theta,p,o}} \sum_{\theta} \sum_{p}^{\mathrm{H,V}} \sum_{o}^{\mathrm{A,D}} (1 - \mathrm{KGE}_{\theta,p,o}) + W_{\alpha} \frac{1}{N_{\alpha}} \sum_{i}^{N_{\alpha}} N_{\alpha} \frac{(\alpha_{0,i} - \alpha_i)^2}{\sigma^2_{\alpha_{0,i}}}, \tag{9}$$

with:

$$\mathrm{KGE}_{\theta,p,o} = 1 - \sqrt{W_1 \left(1 - \mathrm{R}_{\theta,p,o}\right)^2 + W_2 \left(1 - \mathrm{MR}_{\theta,p,o}\right)^2 + W_3 \left(1 - \mathrm{SR}_{\theta,p,o}\right)^2}, \tag{10}$$

where $N_{\theta,p,o}$ is the number of combinations of incidence angle bins θ, polarizations p and orbits o, while N_α refers to the number of calibrated RTM parameters. W_{KGE} and W_α are weight-factors for the different penalty terms, respectively set to 100 and 1. The latter values have been selected to put less constrain on the parameter penalty compared to the KGE. Further, $\mathrm{KGE}_{\theta,p,o}$ is the KGE for a specific θ, p and o. R is the correlation coefficient, MR the ratio between the mean of the simulations and the mean of the observations, and SR the ratio between the standard deviation of the simulations and the standard deviation of the observations. Note that the latter three criteria should ideally equal to 1, through which the KGE becomes 1. W_1 to W_3 are weights that can be assigned to specify the relative importance of the different criteria for the problem at hand. Although different weights have been tested, the aim of this study is not to perform a thorough optimization of the weights. Such optimization is a complex task and truly depends on the specific objectives of the calibration. Therefore, these weights are adopted as an indication of what could be possible. In this specific study, the weights have been set to $W_1 = 0.05$, $W_2 = 1.95$ and $W_3 = 0$. The weights W_1 and W_2 were chosen such that emphasis is given to the optimization of the MR, in order to mitigate biases. W_3 is set to 0, as the improvement in SR comes at the expense of an increase in bias. Moreover, as the SR simultaneously embeds the variability of TB in a temporal and spatial context (different grid cells and time steps are contained in the calibration set), compensating effects, e.g. increasing spatial variability at the expense of temporal variability needed to be avoided. Hence, SR is arguably less paramount to the optimization compared to R and MR. Finally, note that the cost function does not account for uncertainties in the observations, through which the calibration could possibly be prone to overfitting. However, no clear evidence of overfitting was observed in this study.

Besides the KGE, the objective function also minimizes parameter (α_i) deviations from initial values ($\alpha_{0,i}$) to account for equifinality, i.e. to select a single optimal parameter set from multiple parameter sets that yield a similar KGE. The deviation term is limited by the variance of a uniform distribution with boundaries $[\alpha_{\min}, \alpha_{\max}]$, given by:

$$\sigma^2_{\alpha_{0,i}} = \frac{(\alpha_{\max,i} - \alpha_{\min,i})^2}{12}. \tag{11}$$

The initial parameter values have been taken from the baseline parameter set given in Table 1. The boundaries of the different parameters are given in Table 2 and indicate both the limits of the search area and the expected uncertainty in the prior parameter estimates. Thereby, it should be noted that Nr_p was not constrained to an initial guess, i.e. the boundaries on Nr_p are only an indication of the search space limits. The reason therefore is the large variability of Nr_p observed from experimental data (Wigneron et al. 2001).

The restriction to a realistic range of parameter values and the prior penalty term together preserve a realistic model sensitivity of TB to SM. This sensitivity is generally known to be an approximate 2–3 K increase in TB for a 0.01 $\mathrm{m^3m^{-3}}$ decrease in soil moisture around 40° incidence angle for low vegetation (Jackson 1993). As denoted in De Lannoy et al. (2013), the sensitivity can largely decrease if, for instance, unrealistically high values for roughness and optical depth are used. In this case, the emission from the soil is very low and thus TB sensitivity to SM is very low. Such unrealistic parameter values could be obtained due to compensating effects during the calibration.

c. *Calibration experiments*

A set of calibration case studies (Table 3) were performed in order to investigate several aspects in the RTM optimization. A first numerical experiment aims at investigating the impact of the SM climatology, which is generally characteristic to the LSM, on the TB simulations with baseline RTM parameters. To this end, a cumulative distribution function (CDF) matching step was applied to convert the VIC SM output to the climatology of the SMOS Level 3 SM retrievals. Note that this study refrains from providing recommendations on the optimal SM climatology (e.g. LSM versus SMOS), but rather aims at identifying its impact in view of RTM optimization for SMOS. The experiment where CDF-matched soil moisture is used as input to CMEM, without RTM parameter calibration, is referred to as case 1 in Table 3. The CDFs were computed using the non-parametric kernel-based method by Li et al. (2010). Thereby, SM values from the year 2010 were used to calculate the CDF matching coefficients between VIC and SMOS on a pixel-basis, which were subsequently used to rescale the VIC SM for the year 2011. Figure 2 (a) shows a comparison between the SM densities from SMOS and VIC before CDF matching, revealing a bias of $0.17\,\mathrm{m}^3\ \mathrm{m}^{-3}$ and correlation of 0.42. Notably, the VIC SM displays a decreased dynamic range compared to the SMOS retrievals. Figure 2 (b) shows how the CDF matching reduces the bias to $0.01\,\mathrm{m}^3\ \mathrm{m}^{-3}$ and increases the correlation to 0.75 for the 2011 validation data set.

In Table 3, cases 2 to 6 investigate the improvements in TB simulation after calibrating specific RTM parameters. Given the large impact of roughness on the climatological mean TB (De Lannoy et al. 2013), the h parameter is included in all cases. Case 2 explores the calibration of h only, whereas case 3 to 5 simultaneously retrieve Nr, τ, or b_1 and b_2, respectively. Further, case 6 demonstrates the added value of a joint calibration of h, Nr and τ. Calibration cases 2 to 6 are performed on a data set which includes both ascending and descending overpasses, as well as both H and V polarizations. Thus, no polarization-dependent parameters are considered in these cases.

Furthermore, cases 7 to 10 are designed to investigate the effect of the radiometer configuration on the calibration. In this context, it is investigated that a differentiation of the calibration between either polarizations or orbits, or both polarizations and orbits, may enhance the performance of the simulations. Finally, case 10 considers the calibration of a polarization-independent h, and polarization-dependent Nr_p and τ_p parameters, while accounting for ascending and descending orbits separately.

4. Results

a. *Baseline run*

A baseline run with the RTM parameters of Table 1 was performed to simulate the SMOS TB observations over the Upper Mississippi for the year 2011. Figure 3 shows the basin-averaged angular TB signatures for the (a) ascending and (c) descending orbits, comparing the SMOS observations with the VIC+CMEM simulations. As revealed by this figure, a large bias in the order of 30 K for H-pol and between 27 K (at 17.5°) and 10 K (at 52.5°) for V-pol is found for ascending orbits. Descending orbits are exposed to slightly lower biases of approximately 20 K and 5–15 K for H and V polarization, respectively, which are likely attributed to a lower probability of RFI in descending orbits. Figure 3 moreover displays the RMSE and KGE (with weights $W_1 = 0.05$, $W_2 = 1.95$ and $W_3 = 0$) for each angle and polarization, for (b) ascending and (d) descending orbits. In the case of H-pol, the RMSE increases with incidence angle, whereas the opposite trend is observed for V-pol, irrespective of the orbit. The KGE generally follows a similar behavior, with an increase in performance for lower/higher incidence angles in case of H/V-polarization. Finally, the V-polarized simulations outperform the simulations at H-pol, mostly because of lower biases.

Figure 4 shows the 2011 annual mean (a) SMOS retrievals and (b) simulations of SM over the Upper Mississippi Basin, their (c) bias (SMOS minus VIC) and (d) Spearman rank correlation. The comparison reveals a poor spatial agreement in SM patterns, and large wet model bias that ranges between -5 vol% in the South to -30 vol% in the Northwest. Conversely, the correlation coefficient reaches up to 0.7 for most parts of the basin, demonstrating the agreement in temporal variations between SM simulations and retrievals, particularly in the South and Southwest area that are dominated by low vegetation types (see Figure 1). The correlation results are consistent with comparison studies of SMOS SM products using local measurements (Al Bitar et al. 2012; Leroux et al. 2014). The forest area in the Northeast is mainly characterized by a low temporal correlation close to 0. This may be reasoned by the decreased sensitivity of the SMOS L-band TB observations to SM under dense vegetation cover.

Figures 5 and 6 display the 2011 annual mean ascending (a) SMOS TB observations at 42.5° incidence angle, the (b) corresponding VIC+CMEM simulations, their (c) bias and (d) correlation for H- and V-polarization, respectively. Compared to SM, the spatial correspondence between the observations and simulations becomes slightly more prominent, mainly driven by the influences of land cover. The bias is found to be particularly large (up to 50 K) over low vegetated areas at H-pol, whereas biases over forest areas are generally limited within 10 K. These results are consistent with De Lannoy et al. (2013), who found that the use of literature RTM parameters can result in TB biases of 10–50 K against SMOS observations. As for SM, the temporal correlation is especially high in portions dominated with low-vegetation; compared to the SMOS retrievals, the correlations in TB over northern forest areas have increased.

b. Calibration experiments

A set of calibration runs was performed according to Table 3. Table 4 provides an overview of the performance of the different experiments, in comparison to the baseline run during the year 2011. It is important to note that the evaluation criteria in this table are calculated based on datasets combining observations/simulations of different instants in time, spatial locations, and incidence angles. Consequently, regional or seasonal artefacts at specific angle bins are not evaluated by this approach, and will be discussed in Section 4c. In the following, the results of Table 4 are discussed with emphasis on the impact of the LSM SM climatology, the choice of RTM calibration parameters, and the impact of partitioning the calibration between polarizations and orbits.

The importance of the SM climatology is evident when comparing the baseline run with case 1. Averaged over orbits and polarizations, the baseline yields a correlation R of 0.67 and RMSE of 29.72 K, with the bias having an absolute value of 20.27 K (the unbiased RMSE (ubRMSE) is thus 21.73 K, given that: $\text{ubRMSE}^2 = \text{RMSE}^2 - \text{bias}^2$). The corresponding KGE of the baseline equals 0.86. After CDF matching the VIC SM states, the RMSE decreases to 18.85 K, while bias is reduced to 4.69 K. The unbiased RMSE is also slightly reduced to 18.26 K. This demonstrates that most of the bias, and a small part of the mismatch in variability, in the TB simulations is attributed to gross differences in the climatology of the SM simulations of the LSM against SMOS, with the baseline RTM parameters (Table 1) providing a reasonable simulation of TB once the SM climatology difference has been accounted for. The impact of SM climatology and the lack of any established consensus may as well partly explain the large variability in RTM parameters that can be found from modeling studies in literature (e.g. reviewed in De Lannoy et al. (2013)). In addition to a decrease in bias and increase in accuracy, the CDF matching improves the correlation to 0.75 as a consequence of the non-linear relationship between TB and SM. Finally, the KGE is increased from 0.86 to 0.94.

Cases 2 to 5 investigate the calibration of h alone, and h in combination with Nr, τ and b_1 and b_2, respectively. The results show that none of these calibration experiments are able to improve the simulations of case 1. This again justifies the use of baseline RTM parameters as given in Table 1, provided the model SM climatology is corrected. Only for case 6, which investigates the joint calibration of h, Nr, and τ, is a slight improvement obtained. More specifically, the RMSE decreases with 1.5 K, with a minor decrease in bias of 0.2 K. These results are in line with De Lannoy et al. (2013), who observed calibration improvements after increasing the number of calibration parameters (including h and τ).

Given the minor improvements after the joint calibration of h, Nr, and τ, this scenario is further investigated in cases 7 to 10, where independent calibrations for specific polarizations and/or orbits are carried out. It shows that separation of polarizations causes a slightly larger improvement compared to the separation of orbits, whereas treating both polarizations and orbits separately yields the largest improvement. In the latter case, a decrease of 0.6 K in RMSE and approximately 1 K in bias was found in comparison with case 6. Finally, case 10 indicates that there is no clear need to account for polarization differences in the calibration of h. Hence, the calibration case 10 may be proposed as the most optimal.

The improvement after separating ascending (6 am local time) and descending (6 pm local time) orbits may be reasoned by the fact that for ascending orbits, ionospheric effects are expected to be minimal, whereas surface conditions are close to thermal equilibrium. During descending orbits, the temperature gradients can be high (Jackson 1980). Also, the SMOS mission is known to be impacted by RFI (Oliva et al. 2012) and this impact is different for ascending and descending orbits as the instrument is tilted by 32.5° from nadir. The presence of low level RFI in the ascending SMOS observations over Northern America due to the active presence of a military radar system in 2010–2011 was highlighted in Collow et al. (2012) and De Lannoy et al. (2013). Several studies (Bircher et al. 2012; Leroux et al. 2014; Verhoest et al. 2014) have also shown that ascending and descending SMOS data reveal different statistics, supporting the need for different parameterizations. However, a caveat to the differentiation between orbits is the fact that this purposely introduces model bias to match the observation bias. If the objective would be to provide consistent time-independent simulations of TB, a differentiation between orbits may not be advisable. Finally, the use of polarization-dependent surface roughness and (particularly) vegetation parameters may be justified by differences in radiative transfer between polarizations as implemented in the L-MEB model (Wigneron et al. 2001) and validated using local radiometer and SMOS data (Wigneron et al. 2012).

c. Validation of calibration case 10

The calibrated parameters associated with case 10 are further used in a coupled VIC+CMEM model simulation over the Upper Mississippi for 2011. Table 5 shows the parameters obtained for ascending and descending orbits for each land cover class with cover fraction larger than 1%, except for water and urban. The roughness h of low vegetation types (e.g. wooded grassland and cropland) slightly increased, mainly for ascending orbits. The single-scattering albedo τ_p remained close to the baseline for ascending orbits, whereas a slight increase is observed for descending orbits. Furthermore, values for low vegetation are found to be larger than zero for all polarizations and orbits. Finally, large differences are occurring in Nr_p even within classes of low and high vegetation types as this parameter was not constrained towards the initial parameter values. Nevertheless, the H-pol results may indicate a sub-optimal performance of the initial value (equal to 2 for all vegetation types), as calibrated values are mostly in the range of $[0, 1]$. For V-pol, it is less clear to which values the calibration is converging.

To demonstrate the improvements made with respect to the baseline, Figure 7 shows the angular signature for the 2011 validation data set. In comparison with Figure 3, it clearly shows a reduction in bias ($< 10\,\mathrm{K}$) over all angle bins. Furthermore, the RMSE decreases significantly to less than 20 K in all cases, whereas the KGE increases to above 0.9. Finally, after the RTM optimization, the TB simulations show a comparable accuracy (RMSE, KGE) over all angles, which was not the case for the baseline simulations (see Figure 3).

Figures 8 and 9 show a comparison between the simulations and observations of the mean 2011 ascending TB at 42.5° incidence angle, after SM CDF matching and RTM calibration, for H- and V-polarization respectively. Although the basin average TB bias remains well below 5 K, considerable regional biases are still encountered. Particularly for H-polarization, the simulated TBs in the Northwest show a warm model bias compared to the SMOS observations, whereas the opposite is true in the Southwest. Since large parts of these two regions share the same dominant land cover type (i.e. cropland), whilst the soil moisture bias has been almost completely removed through CDF matching, the remaining cause for the observed systematic differences can be found in measurement errors, systematic forcing errors (e.g. precipitation), or the characterization of the vegetation. Specifically for vegetation, the Level 3 SMOS retrievals employ static land use maps from ECOCLIMAP and related LAI. Based on this information, the optical thickness of the vegetation is dynamically retrieved in conjunction with soil moisture (Kerr et al. 2012). In the case of VIC, the land cover is sourced from the UMD, with fixed monthly LAI parameters based on AVHRR satellite data. Consequently, regional differences in vegetation characterization may cause biases in TB, notwithstanding the unbiased soil moisture fields. Further removal of the regional bias would require pixel-based RTM calibration, or post-processing, e.g. through CDF matching of the TB simulations or observations. However, it should be recalled that the present study does not apply pixel-based calibration in order to preserve the sub-grid vegetation variability of VIC and simplify the coupling with the RTM. Finally, the Spearman rank correlation between the observations and simulations of TB is found to be particularly high over low vegetation, with R-values up to 0.9. Moreover, the correlation has increased after applying the SM CDF matching, as seasonal TB discrepancies have been reduced through adjusting SM which non-linearly relates to TB.

Figure 10 displays maps of R, MR, SR, and KGE, averaged over all angle bins, polarizations and orbits. In this case, the KGE has been calculated with weights (W_1 to W_3) equal to 1. The choice of equal weights is motivated by the fact that SR is considered a valuable criterion for pixel-based evaluation; no compensating effects can occur, e.g. due to the embedding of spatial variability as in the calibration objective function. Again, the correlation coefficients are high over areas dominated by low vegetation, whereas slightly lower correlations are found in forest areas mainly in the North. The bias is low over most parts, however, a warm model bias (ratio of simulations over observations) is found in the North-western cropland area, whereas a cold bias is observed in the South, dominated by cropland and wooded grassland. The ratio of the standard deviation shows a large contrast between low and high vegetation. While SR is close to one for low vegetation, a large underestimation of the TB variability is observed over forests. This may arguably be related to shortcomings of the model in the characterization of the surface emission and penetration depth over forest areas. As can be seen in Figure 10 (d), the KGE is mainly influenced by R and SR, showing lower efficiencies in the forested Northeast. Nevertheless, the KGE demonstrates the ability for accurately simulating TBs over low vegetation, with efficiencies between 0.6 and 0.8.

Finally, time series for 2011 of simulated and observed TB are shown in Figure 11, for ascending orbits at 42.5°, at H- and V-polarization. The time series have been obtained for a SMOS pixel (lat = 42.8260°, lon = -91.1060°) covered for 82% by forest types and another pixel (lat = 40.2180°, lon = -88.5030°) covered for 95% by cropland. As was also revealed by Figure 10, the forest simulations lack the temporal variability observed by SMOS, although seasonal patterns are captured well. Also, some of the SMOS observations might still be affected by errors such as those caused by RFI (e.g. the high TB-H observation at DOY 150). A slight overestimation by VIC+CMEM is still observed in winter months for H-polarization, whereas summer TBs are slightly underestimated at V-polarization. Nevertheless, it should be noted that this figure provides an example for only one forest pixel. Hence, findings for this specific location are not necessarily true for other pixels dominated by forest cover. Over cropland, the simulations at both H- and V-polarization generally show a good correspondence with the SMOS observations. In this case, observations and simulations are characterized by high correlation and low bias, while exposing similar levels of variability.

5. Conclusions

To facilitate the direct assimilation of multi-angular/polarization SMOS TB observations, the Community Microwave Emission Modelling platform (CMEM) was coupled to the VIC land surface model. Such direct assimilation of TB observations can be of high value in time-constrained forecasting applications, e.g. of hydrologic events, as it circumvents the need for SM retrieval data that are generally provided with longer time-lag. However, the coupling of an LSM with RTM poses significant challenges when the objective is to simulate accurate and un-biased TBs in comparison with SMOS observations. This study shows that propagation of the VIC soil moisture and surface temperature fields through CMEM, using literature-based RTM parameters, may cause biases in TB that locally reach up to 50 K, with an average of about 30 K. A number of experiments were conducted in order to mitigate biases and improve the accuracy of the simulations.

The VIC SM is found to show mean annual discrepancies with the corresponding SMOS retrievals in the range of 10 to 30 vol%. Hence, optimization of the RTM using the direct SM output from VIC may lead to parameter combinations that decrease the sensitivity of TB to SM, thus motivating the rescaling of VIC SM. After rescaling the VIC SM to the climatology of SMOS through CDF matching, the average TB bias reduced to less than 5 K, even with literature-based RTM parameterization. In addition to mitigating biases, the CDF matching of SM also increased the temporal correlation between the TB observations and simulations, as a result of the non-linear relation of TB to SM. This demonstrates that the literature parameters, which are also employed in the operational SMOS retrieval algorithm, provide a realistic characterization of the surface and vegetation. Furthermore, it shows that in the case of L-band brightness temperature assimilation, some bias correction to the LSM SM state may be needed.

Through a series of RTM calibration experiments, optimal calibration parameters and associated RTM parameter values were selected for each land cover class present in the Upper Mississippi Basin. The calibration of surface roughness h alone, or in combination with either the angular dependence, Nr, the scattering albedo, τ, or the vegetation optical depth (b_1 and b_2) parameters, did not further improve the performance of the simulations. Only a combination of three calibration parameters, i.e., h, Nr and τ, slightly decreased the RMSE (17.36 K) and bias (4.48 K) of the TB simulations. Further improvements in RMSE (16.68 K) and bias (3.79 K) were achieved by separating the calibration for H- and V-polarization, and ascending and descending orbits.

A spatio-temporal analysis of the optimized TB simulations over the Upper Mississippi Basin revealed that regional biases (up to 20 K) are still unresolved, particularly in the North-western cropland area, and wooded grassland area in the South. This may be attributed to differences in the characterization of vegetation between the LSM and the SMOS retrieval algorithm. However, most other areas were characterized by low bias (<5 K). Finally, the simulations over forest were found to lack the variability observed by SMOS over short time scales. In combination with lower temporal correlations, forest areas were therefore characterized by lower values of the KGE, which is a combined measure for correlation, bias and variability. For most cropland and low vegetation areas, the coupled model was found to provide accurate and unbiased TB simulations, characterized by KGE values of 0.6 to 0.8, which is a prerequisite for the assimilation of SMOS TB observations to benefit hydrologic applications.

Acknowledgments.

The work has been performed in the framework of the ESA-ITT project 'SMOS+Hydrology Study' and was partly funded through project SR/02/152 ('FloodMoist') financed by the Belgian Science Policy (BELSPO), and the CNES Terre, Océan, Surfaces Continentales, Atmosphère (TOSCA) programme. Hans Lievens is a postdoctoral research fellow of the Research Foundation Flanders (FWO).

REFERENCES

Al Bitar, A., D. Leroux, Y. H. Kerr, O. Merlin, P. Richaume, A. Sahoo, and E. F. Wood, 2012: Evaluation of SMOS soil moisture products over continental US using the SCAN/SNOTEL network. *IEEE Transactions on Geoscience and Remote Sensing*, **50 (5)**, 1572–1586.

Balsamo, G., J.-F. Mahfouf, S. Belair, and G. Deblonde, 2006: A global root-zone soil moisture analysis using simulated L-band brightness temperature in preparation for the hydros satellite mission. *Journal of Hydrometeorology*, **7 (5)**, 1126–1146.

Bircher, S., N. Skou, K. H. Jensen, J. P. Walker, and L. Rasmussen, 2012: A soil moisture and temperature network for SMOS validation in Western Denmark. *Hydrology and Earth System Sciences*, **16 (5)**, 1445–1463.

Choudhury, B., T. Schmugge, A. Chang, and R. Newton, 1979: Effect of surface roughness on the microwave emission from moist soils. *Journal of Geophysical Research-Atmospheres*, **84 (NC9)**, 5699–5706.

Collow, T. W., A. Robock, J. B. Basara, and B. G. Illston, 2012: Evaluation of SMOS retrievals of soil moisture over the central United States with currently available in situ observations. *Journal of Geophysical Research-Atmospheres*, **117**.

Cosgrove, B., et al., 2003: Real-time and retrospective forcing in the North American Land Data Assimilation System (NLDAS) project. *Journal of Geophysical Research-Atmospheres*, **108 (D22)**.

Crow, W. T. and E. F. Wood, 2003: The assimilation of remotely sensed soil brightness temperature imagery into a land surface model using ensemble Kalman filtering: A case study based on ESTAR measurements during SGP97. *Advances in Water Resources*, **26 (2)**, 137 – 149.

De Lannoy, G. J. M., P. R. Houser, V. R. N. Pauwels, and N. E. C. Verhoest, 2007: State and bias estimation for soil moisture profiles by an ensemble Kalman filter: Effect of assimilation depth and frequency. *Water Resources Research*, **43 (6)**.

De Lannoy, G. J. M., R. H. Reichle, and V. R. N. Pauwels, 2013: Global calibration of the GEOS-5 L-band microwave radiative transfer model over nonfrozen land using SMOS observations. *Journal of Hydrometeorology*, **14 (3)**, 765–785.

de Rosnay, P., et al., 2009: AMMA Land Surface Model Intercomparison Experiment coupled to the Community Microwave Emission Model: ALMIP-MEM. *Journal of Geophysical Research-Atmospheres*, **114**.

Draper, C., R. Reichle, R. de Jeu, V. Naeimi, R. Parinussa, and W. Wagner, 2013: Estimating root mean square errors in remotely sensed soil moisture over continental scale domains. *Remote Sensing of Environment*, **137**, 288–298.

Drusch, M., T. Holmes, P. de Rosnay, and G. Balsamo, 2009: Comparing ERA-40-based L-band brightness temperatures with Skylab observations: A calibration/validation study using the Community Microwave Emission Model. *Journal of Hydrometeorology*, **10 (1)**, 213–226.

Entekhabi, D., et al., 2010: The Soil Moisture Active Passive (SMAP) mission. *Proceedings of the IEEE*, **98 (5)**, 704–716.

Escorihuela, M. J., A. Chanzy, J. P. Wigneron, and Y. H. Kerr, 2010: Effective soil moisture sampling depth of L-band radiometry: A case study. *Remote Sensing of Environment*, **114 (5)**, 995–1001.

Gao, H., T. J. Jackson, M. Drusch, and R. Bindlish, 2006: Using TRMM/TMI to retrieve surface soil moisture over the southern United States form 1998 to 2002. *Journal of Hydrometeorology*, **7 (1)**, 23–38.

Gupta, H. V., H. Kling, K. K. Yilmaz, and G. F. Martinez, 2009: Decomposition of the mean squared error and NSE performance criteria: Implications for improving hydrological modelling. *Journal of Hydrology*, **377 (1–2)**, 80–91.

Gutman, G. and A. Ignatov, 1998: The derivation of the green vegetation fraction from NOAA/AVHRR data for use in numerical weather prediction models. *International Journal of Remote Sensing*, **19 (8)**, 1533–1543.

Han, X., H.-J. Hendricks-Franssen, X. Li, Y. Zhang, C. Montzka, and H. Vereecken, 2013: Joint assimilation of surface temperature and L-band microwave brightness temperature in land data assimilation. *Vadose Zone Journal*, **12 (3)**.

Hansen, M., R. Defries, J. Townshend, and R. Sohlberg, 2000: Global land cover classification at 1km spatial resolution using a classification tree approach. *International Journal of Remote Sensing*, **21 (6-7)**, 1331–1364.

Holmes, T. R. H., M. Drusch, J.-P. Wigneron, and R. A. M. de Jeu, 2008: A global simulation of microwave emission: Error structures based on output from ECMWF's operational integrated forecast system. *IEEE Transactions on Geoscience and Remote Sensing*, **46 (3)**, 846–856.

Jackson, T., 1980: Profile soil moisture from surface measurements. *Journal of the Irrigation and Drainage Division-ASCE*, **106 (2)**, 81–92.

Jackson, T., 1993: Measuring surface soil moisture using passive microwave remote sensing. *Hydrological Processes*, **7 (2)**, 139–152.

Jacquette, E., A. Al Bitar, A. Mialon, Y. Kerr, A. Quesney, F. Cabot, and P. Richaume, 2010: SMOS CATDS level 3 global products over land. *Remote Sensing for Agriculture, Ecosystems, and Hydrology XII*, Neale, CMU and Maltese, A, Ed., Proceedings of SPIE-The International Society for Optical Engineering, Vol. 7824, Conference on Remote Sensing for Agriculture, Ecosystems, and Hydrology XII, Toulouse, France.

Kennedy, J. and R. Eberhart, 1995: Particle swarm optimization. *IEEE International Conference on Neural Networks Proceedings, Vols 1-6*, 1942–1948, 1995 IEEE International Conference on Neural Networks (ICNN 95), Perth, Australia.

Kerr, Y. H., P. Waldteufel, J. P. Wigneron, J. M. Martinuzzi, J. Font, and M. Berger, 2001: Soil moisture retrieval from space: The Soil Moisture and Ocean Salinity (SMOS) mission. *IEEE Transactions on Geoscience and Remote Sensing*, **39 (8)**, 1729–1735.

Kerr, Y. H., et al., 2012: The SMOS soil moisture retrieval algorithm. *IEEE Transactions on Geoscience and Remote Sensing*, **50 (5)**, 1384–1403.

Leroux, D. J., Y. H. Kerr, A. Al Bitar, R. Bindlish, T. J. Jackson, B. Berthelot, and G. Portet, 2014: Comparison between SMOS, VUA, ASCAT, and ECMWF soil moisture products over four watersheds in US. *IEEE Transactions on Geoscience and Remote Sensing*, **52 (3)**, 1562–1571.

Li, H., J. Sheffield, and E. F. Wood, 2010: Bias correction of monthly precipitation and temperature fields from Intergovernmental Panel on Climate Change AR4 models using equidistant quantile matching. *Journal of Geophysical Research-Atmospheres*, **115**.

Liang, X., D. Lettenmaier, E. Wood, and S. Burges, 1994: A simple hydrologically based model of land-surface water and energy fluxes for general-circulation models. *Journal of Geophysical Research-Atmospheres*, **99 (D7)**, 14 415–14 428.

Liang, X., E. Wood, and D. Lettenmaier, 1996: Surface soil moisture parameterization of the VIC-2L model: Evaluation and modification. *Global Planetary Change*, **13 (1–4)**, 195–206.

Liang, X., E. Wood, and D. Lettenmaier, 1999: Modeling ground heat flux in land surface parameterization schemes. *Journal of Geophysical Research-Atmospheres*, **104 (D8)**, 9581–9600.

Maurer, E., G. O'Donnell, D. Lettenmaier, and J. Roads, 2001: Evaluation of the land surface water budget in NCEP/NCAR and NCEP/DOE reanalyses using an off-line hydrologic model. *Journal of Geophysical Research-Atmospheres*, **106 (D16)**, 17 841–17 862.

Maurer, E., A. Wood, J. Adam, D. Lettenmaier, and B. Nijssen, 2002: A long-term hydrologically based dataset of land surface fluxes and states for the conterminous United States. *Journal of Climate*, **15 (22)**, 3237–3251.

Miller, D. and R. White, 1998: A conterminous united states multilayer soil characteristics dataset for regional climate and hydrology modeling. *Earth Interactions*, **2 (1)**, 1–26.

Mironov, V., M. Dobson, V. Kaupp, S. Komarov, and V. Kleshchenko, 2004: Generalized refractive mixing dielectric model for moist soils. *IEEE Transactions on Geoscience and Remote Sensing*, **42 (4)**, 773–785.

Mitchell, K., et al., 2004: The multi-institution North American Land Data Assimilation System (NLDAS): Utilizing multiple GCIP products and partners in a continental distributed hydrological modeling system. *Journal of Geophysical Research-Atmospheres*, **109 (D7)**.

Montzka, C., J. P. Grant, H. Moradkhani, H.-J. Hendricks-Franssen, L. Weihermueller, M. Drusch, and H. Vereecken, 2013: Estimation of radiative transfer parameters from L-band passive microwave brightness temperatures using advanced data assimilation. *Vadose Zone Journal*, **12 (3)**.

Nijssen, B., R. Schnur, and D. Lettenmaier, 2001: Global retrospective estimation of soil moisture using the variable infiltration capacity land surface model, 1980-93. *Journal of Climate*, **14 (8)**, 1790–1808.

Oliva, R., E. Daganzo-Eusebio, Y. H. Kerr, S. Mecklenburg, S. Nieto, P. Richaume, and C. Gruhier, 2012: SMOS radio frequency interference scenario: status and actions taken to improve the RFI environment in the 1400-1427-MHz passive band. *IEEE Transactions on Geoscience and Remote Sensing*, **50 (5)**, 1427–1439.

Pan, M., E. F. Wood, D. B. McLaughlin, D. Entekhabi, and L. Luo, 2009: A multiscale ensemble filtering system for hydrologic data assimilation. Part I: Implementation and synthetic experiment. *Journal of Hydrometeorology*, **10**, 794 – 806.

Pauwels, V. R. N. and G. J. M. De Lannoy, 2011: Multivariate calibration of a water and energy balance model in the spectral domain. *Water Resources Research*, **47**.

Pauwels, V. R. N., R. Hoeben, N. E. C. Verhoest, and F. P. De Troch, 2001: The importance of the spatial patterns of remotely sensed soil moisture in the improvement of discharge predictions for small-scale basins through data assimilation. *Journal of Hydrology*, **251 (1-2)**, 88–102.

Pauwels, V. R. N., R. Hoeben, N. E. C. Verhoest, F. P. De Troch, and P. A. Troch, 2002: Improvement of TOPLATS-based discharge predictions through assimilation of ERS-based remotely sensed soil moisture values. *Hydrological Processes*, **16 (5)**, 995–1013.

Peischl, S., J. P. Walker, D. Ryu, Y. H. Kerr, R. Panciera, and C. Ruediger, 2012: Wheat canopy structure and surface roughness effects on multiangle observations at L-band. *IEEE Transactions on Geoscience and Remote Sensing*, **50 (5)**, 1498–1506.

Pellarin, T., et al., 2003: Two-year global simulation of L-band brightness temperatures over land. *IEEE Transactions on Geoscience and Remote Sensing*, **41 (9)**, 2135–2139.

Reichle, R., R. D. Koster, J. Dong, and A. Berg, 2004: Global soil moisture from satellite observations, land surface models, and ground data: Implications for data assimilation. *Journal of Hydrometeorology*, **5**, 430 – 442.

Reichle, R. H., R. D. Koster, P. Liu, S. P. P. Mahanama, E. G. Njoku, and M. Owe, 2007: Comparison and assimilation of global soil moisture retrievals from the Advanced Microwave Scanning Radiometer for the Earth Observing System (AMSR-E) and the Scanning Multichannel Microwave Radiometer (SMMR). *Journal of Geophysical Research-Atmospheres*, **112 (D9)**.

Reichle, R. H., D. B. McLaughlin, and D. Entekhabi, 2001: Variational data assimilation of microwave radiobrightness observations for land surface hydrology applications. *IEEE Transactions on Geoscience and Remote Sensing*, **39 (8)**, 1708–1718.

Sabater, J. M., P. De Rosnay, and G. Balsamo, 2011: Sensitivity of L-band NWP forward modelling to soil roughness. *International Journal of Remote Sensing*, **32 (19)**, 5607–5620.

Sahoo, A. K., G. J. M. De Lannoy, R. H. Reichle, and P. R. Houser, 2013: Assimilation and downscaling of satellite observed soil moisture over the Little River Experimental Watershed in Georgia, USA. *Advances in Water Research*, **52**, 19 – 33.

Scheerlinck, K., V. R. N. Pauwels, H. Vernieuwe, and B. De Baets, 2009: Calibration of a water and energy balance model: Recursive parameter estimation versus particle swarm optimization. *Water Resources Research*, **45**.

Sheffield, J. and E. F. Wood, 2008: Global trends and variability in soil moisture and drought characteristics, 1950-2000, from observation-driven simulations of the terrestrial hydrologic cycle. *Journal of Climate*, **21 (3)**, 432–458.

Sheffield, J., et al., 2003: Snow process modeling in the North American Land Data Assimilation System (NLDAS): 1. Evaluation of model-simulated snow cover extent. *Journal of Geophysical Research-Atmospheres*, **108 (D22)**.

Verdin, K. and S. Greenlee, 1996: Development of continental scale digital elevation models and extraction of hydrographic features. Presented at the Third International Conference/Workshop on Integrating GIS and Environmental Modelling, National Centre for Geographic Information and Analysis, Santa Fe.

Verhoest, N. E. C., et al., 2014: Copula-based disaggregation of coarse-scale soil moisture observations with implicit bias correction. *IEEE Transactions on Geoscience and Remote Sensing*, *in review*.

Walker, J., G. Willgoose, and J. Kalma, 2001: One-dimensional soil moisture profile retrieval by assimilation of near-surface observations: a comparison of retrieval algorithms. *Advances in Water Resources*, **24 (6)**, 631–650.

Wigneron, J., L. Laguerre, and Y. Kerr, 2001: A simple parameterization of the L-band microwave emission from rough agricultural soils. *IEEE Transactions on Geoscience and Remote Sensing*, **39 (8)**, 1697–1707.

Wigneron, J. P., et al., 2007: L-band Microwave Emission of the Biosphere (L-MEB) Model: Description and calibration against experimental data sets over crop fields. *Remote Sensing of Environment*, **107 (4)**, 639–655.

Wigneron, J.-P., et al., 2012: First evaluation of the simultaneous SMOS and ELBARA-II observations in the Mediterranean region. *Remote Sensing of Environment*, **124**, 26–37.

Wilker, H., M. Drusch, G. Seuffert, and C. Simmer, 2006: Effects of the near-surface soil moisture profile on the assimilation of L-band microwave brightness temperature. *Journal of Hydrometeorology*, **7 (3)**, 433 – 442.

List of Tables

1 The baseline RTM parameters for the UMD land cover types. 33

2 RTM calibration parameters and selected boundaries. 34

3 RTM calibration cases. 35

4 Evaluation of the calibration experiments based on the 2011 validation data set. 36

5 The calibrated RTM parameters of case 10 for the UMD land cover types. 37

Table 1. The baseline RTM parameters for the UMD land cover types.

ID	UMD land cover	Cover [%]	b_1	b_2	Nr_{H}	Nr_{V}	tt_{H}	tt_{V}	h	τ_{H}	τ_{V}
1	Water	1.81	0	0	0	0	0	0	0	0	0
2	Evergreen needleleaf	1.64	0.36	0	2	0	1	1	0.3	0.08	0.08
3	Evergreen broadleaf	0	0.29	0	2	0	1	1	0.3	0.08	0.08
4	Deciduous needleleaf	0	0.36	0	2	0	1	1	0.3	0.08	0.08
5	Deciduous broadleaf	12.93	0.29	0	2	0	1	1	0.3	0.08	0.08
6	Mixed forest	6.61	0.325	0	2	0	1	1	0.3	0.08	0.08
7	Woodland	14.17	0.29	0.03	2	0	1	1	0.3	0.08	0.08
8	Wooded grassland	18.67	0.06	0	2	0	1	1	0.1	0	0
9	Closed shrubland	0	0.06	0	2	0	1	1	0.1	0	0
10	Open shrubland	0	0.06	0	2	0	1	1	0.1	0	0
11	Grassland	0.44	0.06	0	2	0	1	1	0.1	0	0
12	Cropland	42.32	0.06	0	2	0	1	1	0.1	0	0
13	Bare ground	0	0.06	0	2	0	1	1	0.1	0	0
14	Urban and built	1.41	0	0	1	1	0	0	0	0	0

Table 2. RTM calibration parameters and selected boundaries.

Parameter	Min	Max
h	0	2
Nr_{p}	-1	2
τ_{p}	0	0.2
b_1	0	0.7
b_2	0	0.7

Table 3. RTM calibration cases.

Case	Orbits	Polarizations	SM CDF	h	Nr	τ	b_1 and b_2
Baseline	A and D	H and V	No	–	–	–	–
Case 1	A and D	H and V	Yes	–	–	–	–
Case 2	A and D	H and V	Yes	X	–	–	–
Case 3	A and D	H and V	Yes	X	X	–	–
Case 4	A and D	H and V	Yes	X	–	X	–
Case 5	A and D	H and V	Yes	X	–	–	X
Case 6	A and D	H and V	Yes	X	X	X	–
Case 7	A and D	H or V	Yes	X	X	X	–
Case 8	A or D	H and V	Yes	X	X	X	–
Case 9	A or D	H or V	Yes	X	X	X	–
Case 10	A or D	H and/or V	Yes	X	X	X	–

TABLE 4. Evaluation of the calibration experiments based on the 2011 validation data set.

		Baseline	Case 1	Case 2	Case 3	Case 4	Case 5	Case 6	Case 7	Case 8	Case 9	Case 10
A-H	RMSE [K]	40.68	22.03	21.05	19.93	20.72	20.32	19.18	18.95	18.62	18.26	18.10
	Bias [K]	32.43	5.50	3.90	1.92	4.39	1.97	2.05	0.95	-1.79	-2.99	-2.85
	R [−]	0.67	0.76	0.76	0.76	0.76	0.76	0.76	0.76	0.77	0.77	0.76
	KGE [−]	0.79	0.94	0.94	0.95	0.94	0.94	0.95	0.95	0.95	0.94	0.94
A-V	RMSE [K]	24.52	14.25	14.06	14.11	13.72	14.42	13.68	13.97	13.85	13.93	13.66
	Bias [K]	18.75	-3.20	-4.52	-3.58	-3.94	-4.60	-2.53	-1.44	-5.69	-4.07	-4.48
	R [−]	0.70	0.78	0.78	0.78	0.78	0.79	0.78	0.78	0.79	0.79	0.78
	KGE [−]	0.88	0.95	0.95	0.95	0.95	0.95	0.95	0.95	0.94	0.95	0.95
D-H	RMSE [K]	33.92	21.26	20.78	20.29	20.15	20.48	19.46	19.63	18.93	18.49	18.96
	Bias [K]	21.30	-0.86	-2.71	-4.89	-2.09	-4.58	-4.73	-5.85	-1.66	-2.63	-2.46
	R [−]	0.63	0.74	0.74	0.74	0.75	0.74	0.75	0.75	0.75	0.75	0.75
	KGE [−]	0.85	0.94	0.94	0.94	0.94	0.94	0.94	0.93	0.94	0.94	0.94
D-V	RMSE [K]	19.77	17.85	18.28	17.89	17.70	18.53	17.14	16.83	16.39	16.29	15.99
	Bias [K]	8.58	-9.20	-10.76	-9.69	-10.05	-10.65	-8.59	-7.18	-6.36	-4.62	-5.39
	R [−]	0.67	0.73	0.74	0.73	0.74	0.74	0.73	0.73	0.73	0.73	0.72
	KGE [−]	0.91	0.92	0.92	0.92	0.92	0.92	0.92	0.93	0.93	0.93	0.93
Mean	RMSE [K]	29.72	18.85	18.54	18.06	18.07	18.44	17.36	17.34	16.95	16.74	16.68
	|Bias| [K]	20.27	4.69	5.47	5.02	5.12	5.45	4.48	3.85	3.87	3.58	3.79
	R [−]	0.67	0.75	0.76	0.76	0.76	0.76	0.76	0.76	0.76	0.76	0.75
	KGE [−]	0.86	0.94	0.94	0.94	0.94	0.94	0.94	0.94	0.94	0.94	0.94

Table 5. The calibrated RTM parameters of case 10 for the UMD land cover types.

		Ascending					Descending				
ID	UMD land cover	h	Nr_{H}	Nr_{V}	τ_{H}	τ_{V}	h	Nr_{H}	Nr_{V}	τ_{H}	τ_{V}
2	Evergreen needleleaf	0.32	0.85	0.65	0.04	0.12	0.29	0.35	0	0.16	0.11
5	Deciduous broadleaf	0.13	0.48	-0.88	0.07	0.05	0.47	1.67	1.08	0.12	0.13
6	Mixed forest	0.47	0.64	1.19	0.04	0.07	0.33	1.49	0.8	0.15	0.15
7	Woodland	0.09	0.53	0.63	0.09	0.09	0.41	0.62	-0.8	0.11	0.14
8	Wooded grassland	0.29	0.35	1.35	0.01	0.07	0.22	-0.5	0.95	0.05	0.11
12	Cropland	0.26	-0.34	2	0.04	0.03	0.15	1.22	2	0	0.03

List of Figures

1 Land cover map of the Upper Mississippi River basin, following the University of Maryland (UMD) classification (Hansen et al. 2000). 40

2 Density scatter plots between 2011 VIC and SMOS soil moisture [vol%] (a) prior to and (b) after CDF matching. 41

3 The basin averaged angular TB [K] signatures of the SMOS observations and baseline VIC+CMEM simulations for 2011, along with the RMSE [K] and KGE [−] for (a, b) ascending and (c, d) descending orbits, respectively. 42

4 The 2011 annual mean ascending SM [vol%] (a) retrieved from SMOS and (b) simulated by VIC, along with the corresponding (c) bias [vol%] (SMOS minus model) and (d) Spearman rank correlation [−]. 43

5 The 2011 annual mean ascending TB_H [K] at 42.5° (a) observed by SMOS and (b) simulated by the baseline VIC+CMEM, along with the corresponding (c) bias [K] (SMOS minus model) and (d) Spearman rank correlation [−]. 44

6 The 2011 annual mean ascending TB_V [K] at 42.5° (a) observed by SMOS and (b) simulated by the baseline VIC+CMEM, along with the corresponding (c) bias [K] (SMOS minus model) and (d) Spearman rank correlation [−]. 45

7 The basin averaged angular TB [K] signatures of the SMOS observations and calibrated (case 10) VIC+CMEM simulations for 2011, along with the RMSE [K] and KGE [−] for (a, b) ascending and (c, d) descending orbits, respectively. 46

8 The 2011 annual mean ascending TB_H [K] at 42.5° (a) observed by SMOS and (b) simulated by the calibrated (case 10) VIC+CMEM, along with the corresponding (c) bias [K] (SMOS minus model) and (d) Spearman rank correlation [−]. 47

9 The 2011 annual mean ascending TB_V [K] at 42.5° (a) observed by SMOS and (b) simulated by the calibrated (case 10) VIC+CMEM, along with the corresponding (c) bias [K] (SMOS minus model) and (d) Spearman rank correlation [−]. 48

10 The 2011 annual mean (a) correlation [−], (b) mean ratio [−], (c) standard deviation ratio [−] and (d) KGE [−] between SMOS TB and simulated TB (case 10) across all incidence angles, polarizations and orbits. 49

11 2011 time series of ascending TB [K] at 42.5° as observed by SMOS and simulated by VIC+CMEM (case 10), over (a, b) forest and (c, d) cropland grid cells, at (a, c) H-polarization and (b, d) V-polarization. 50

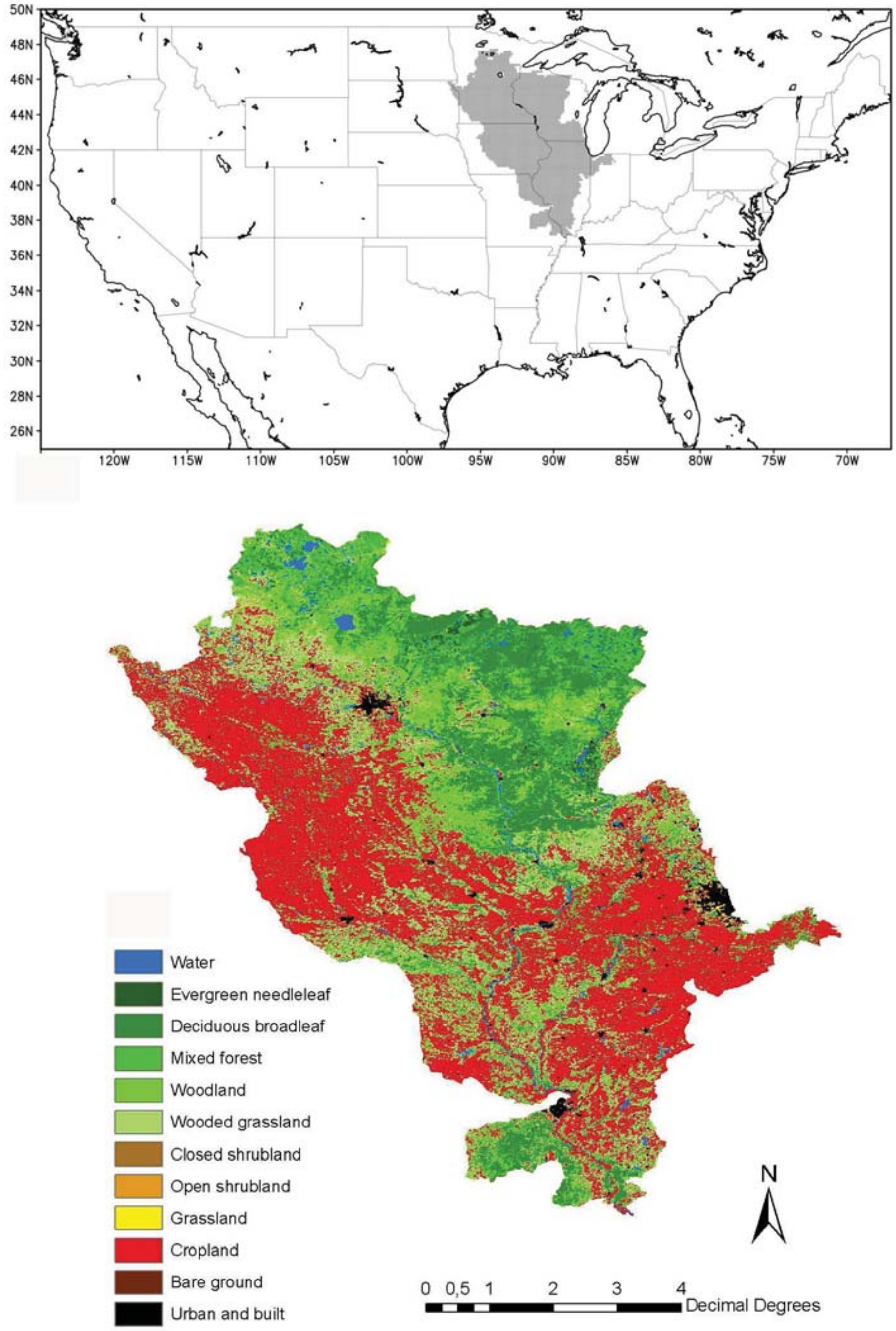

FIG. 1. Land cover map of the Upper Mississippi River basin, following the University of Maryland (UMD) classification (Hansen et al. 2000).

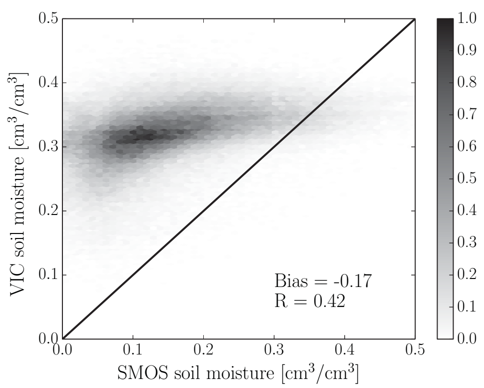

(a)

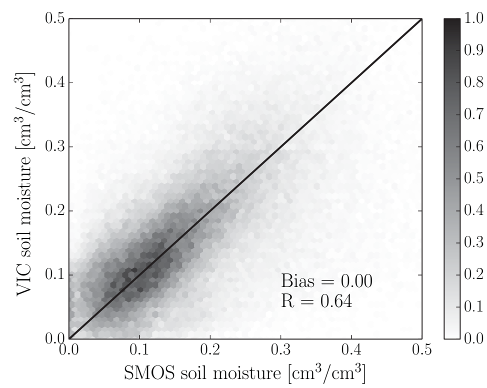

(b)

Fig. 2. Density scatter plots between 2011 VIC and SMOS soil moisture [vol%] (a) prior to and (b) after CDF matching.

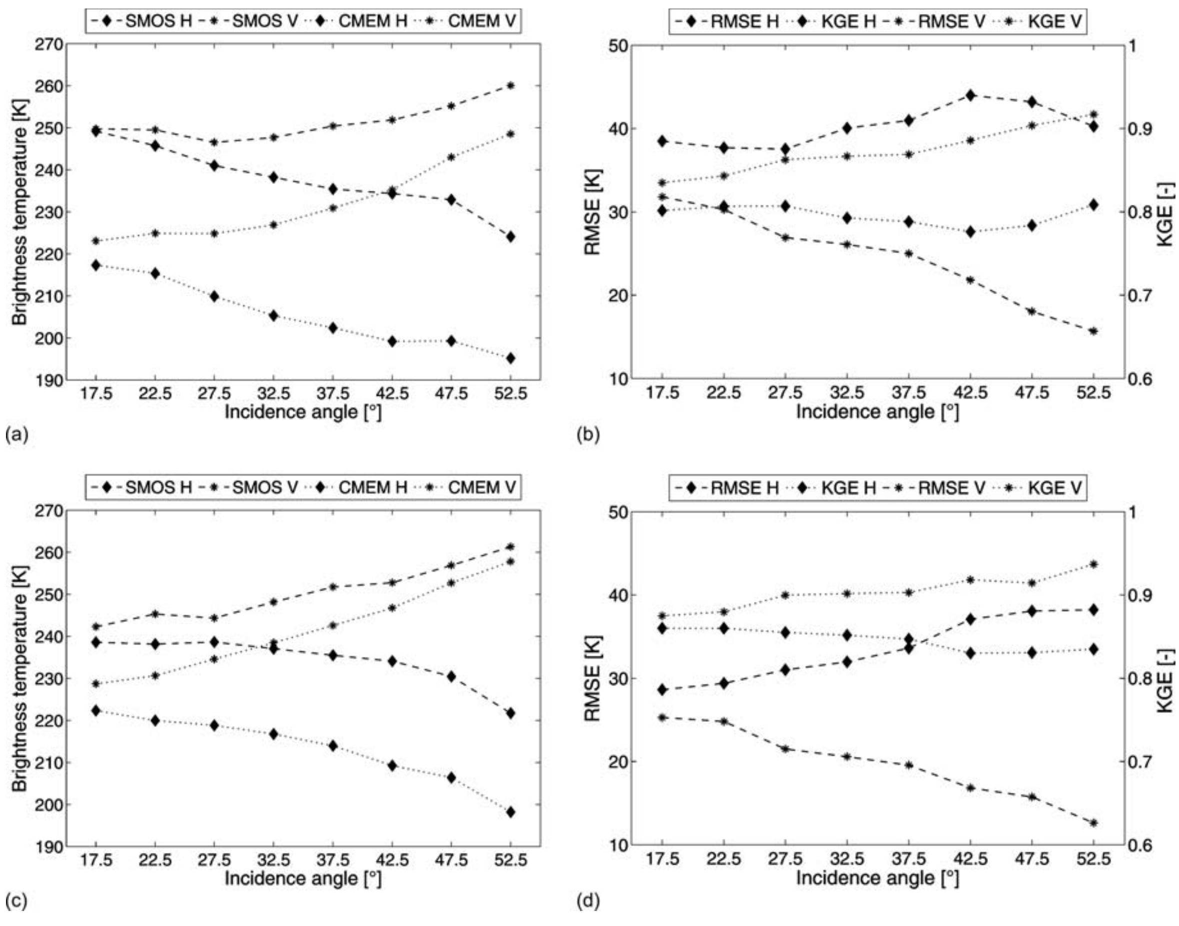

Fig. 3. The basin averaged angular TB [K] signatures of the SMOS observations and baseline VIC+CMEM simulations for 2011, along with the RMSE [K] and KGE [−] for (a, b) ascending and (c, d) descending orbits, respectively.

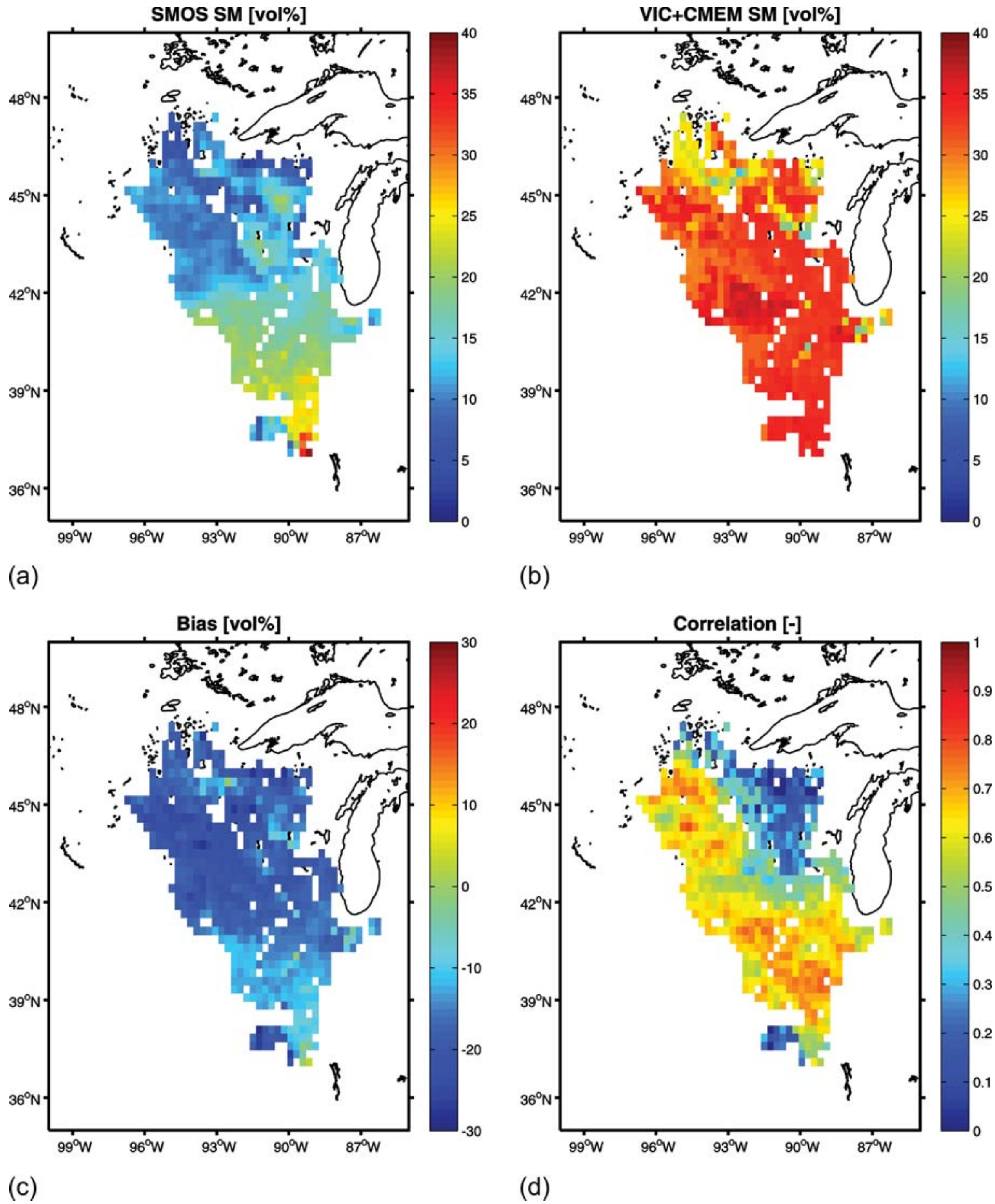

FIG. 4. The 2011 annual mean ascending SM [vol%] (a) retrieved from SMOS and (b) simulated by VIC, along with the corresponding (c) bias [vol%] (SMOS minus model) and (d) Spearman rank correlation [−].

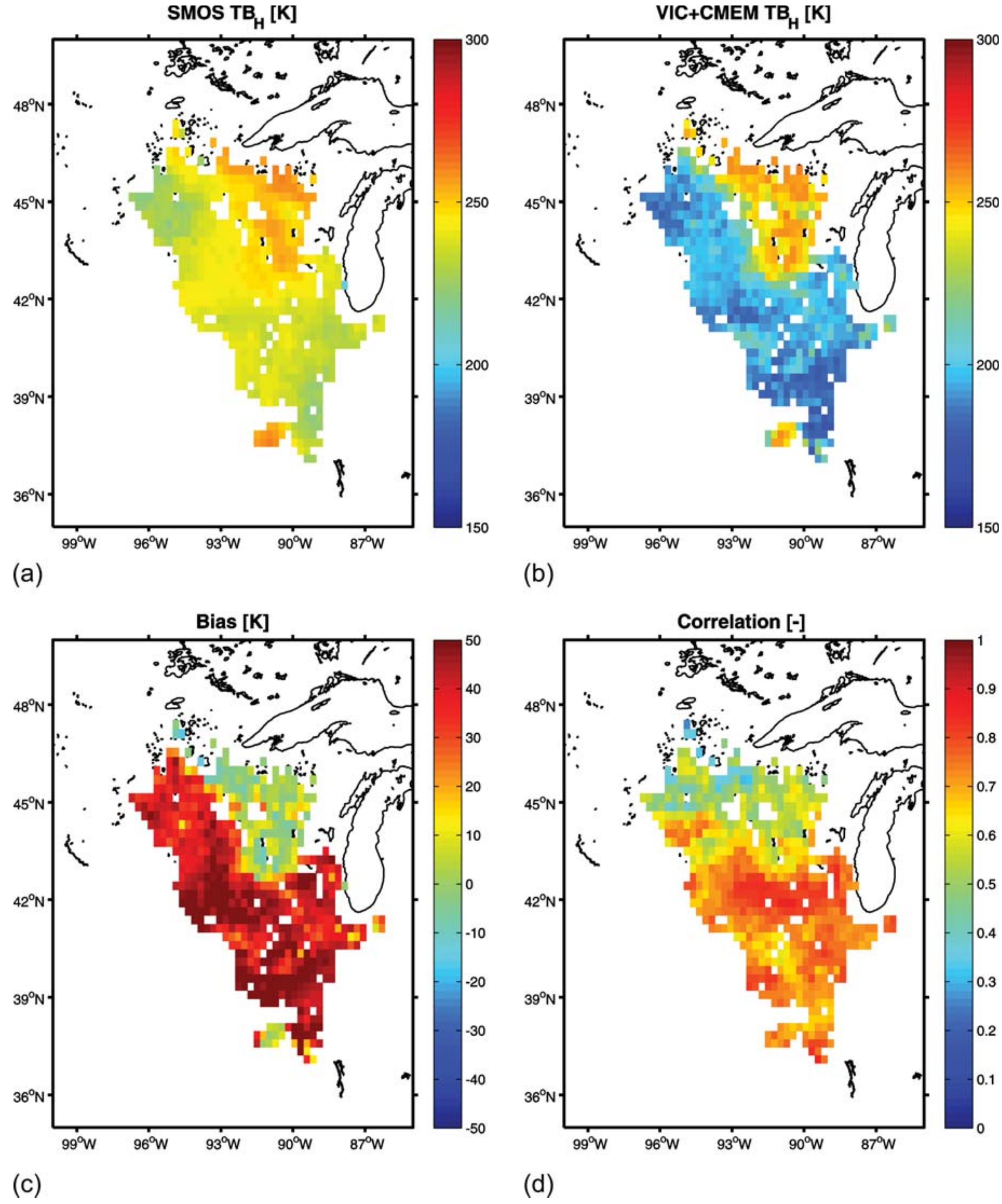

Fig. 5. The 2011 annual mean ascending TB_H [K] at 42.5° (a) observed by SMOS and (b) simulated by the baseline VIC+CMEM, along with the corresponding (c) bias [K] (SMOS minus model) and (d) Spearman rank correlation [−].

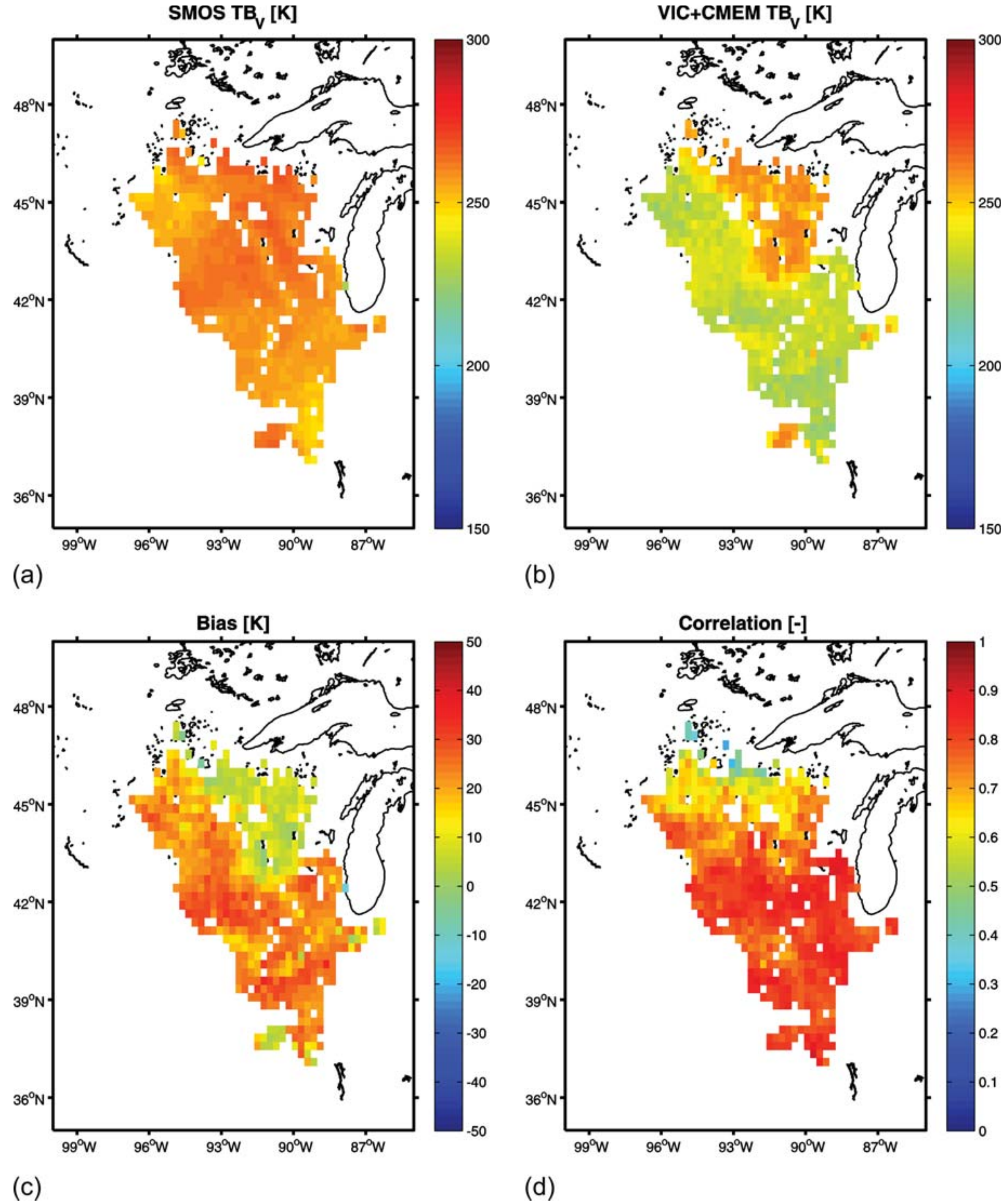

FIG. 6. The 2011 annual mean ascending TB_V [K] at 42.5° (a) observed by SMOS and (b) simulated by the baseline VIC+CMEM, along with the corresponding (c) bias [K] (SMOS minus model) and (d) Spearman rank correlation [−].

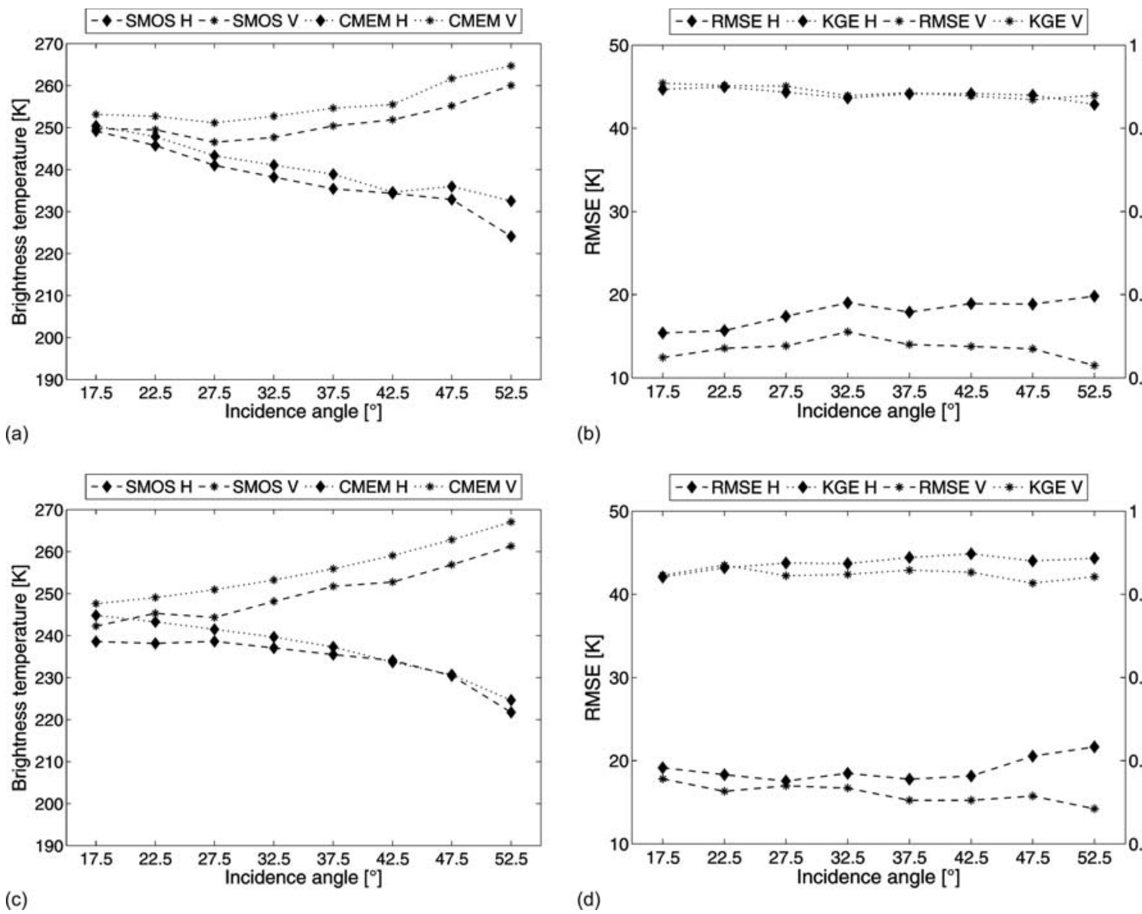

FIG. 7. The basin averaged angular TB [K] signatures of the SMOS observations and calibrated (case 10) VIC+CMEM simulations for 2011, along with the RMSE [K] and KGE [−] for (a, b) ascending and (c, d) descending orbits, respectively.

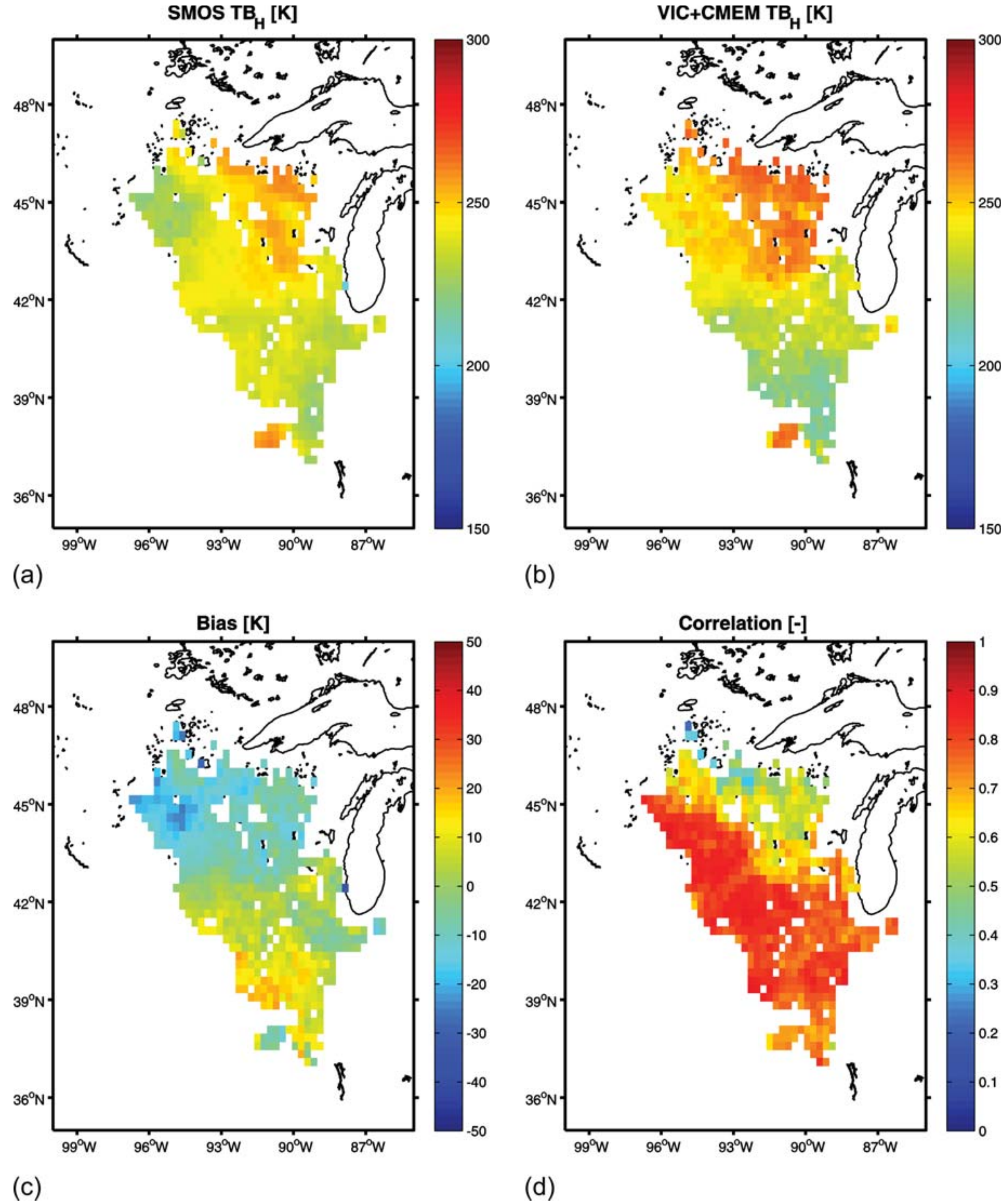

Fig. 8. The 2011 annual mean ascending TB_H [K] at 42.5° (a) observed by SMOS and (b) simulated by the calibrated (case 10) VIC+CMEM, along with the corresponding (c) bias [K] (SMOS minus model) and (d) Spearman rank correlation [−].

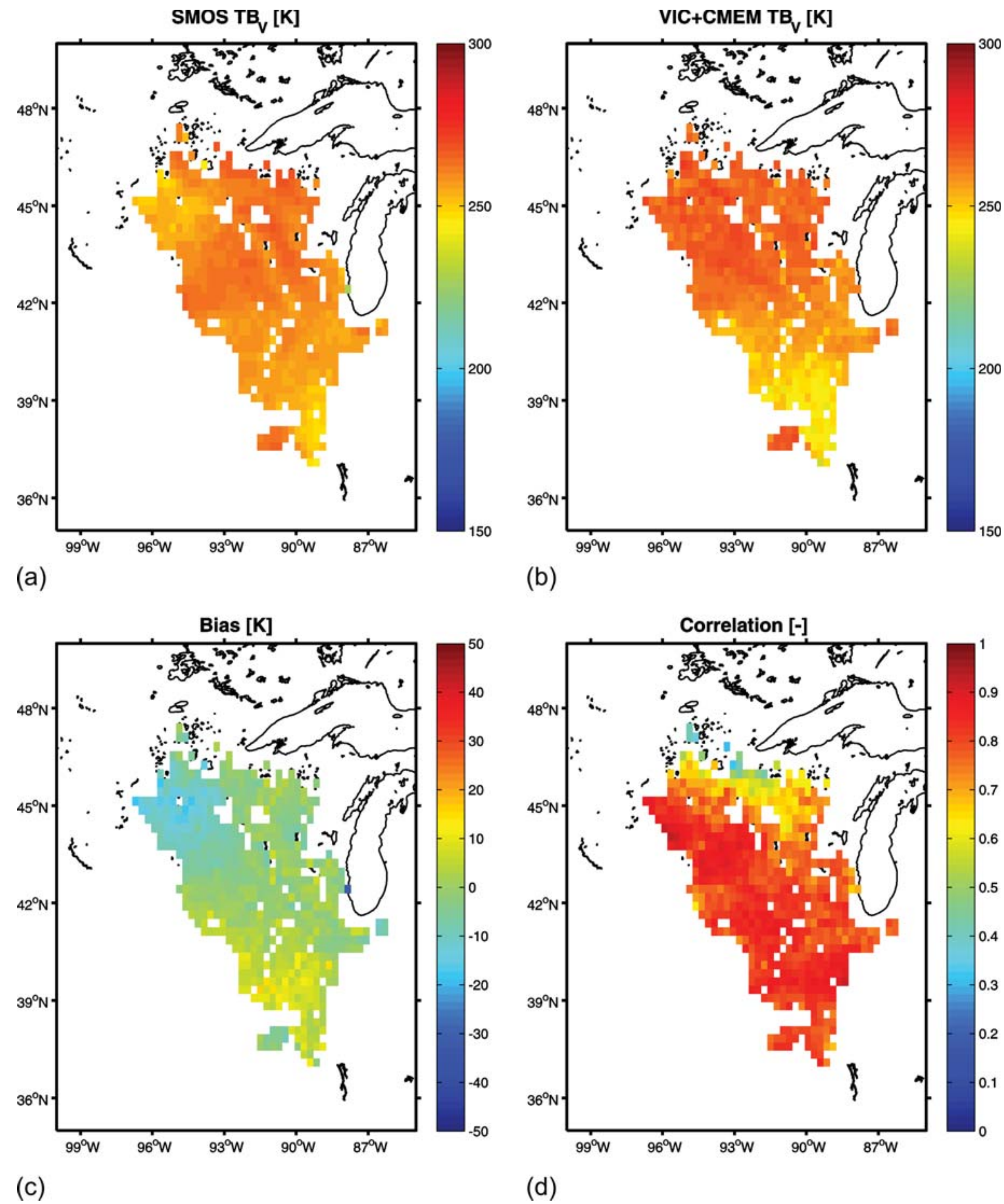

FIG. 9. The 2011 annual mean ascending TB_V [K] at 42.5° (a) observed by SMOS and (b) simulated by the calibrated (case 10) VIC+CMEM, along with the corresponding (c) bias [K] (SMOS minus model) and (d) Spearman rank correlation [−].

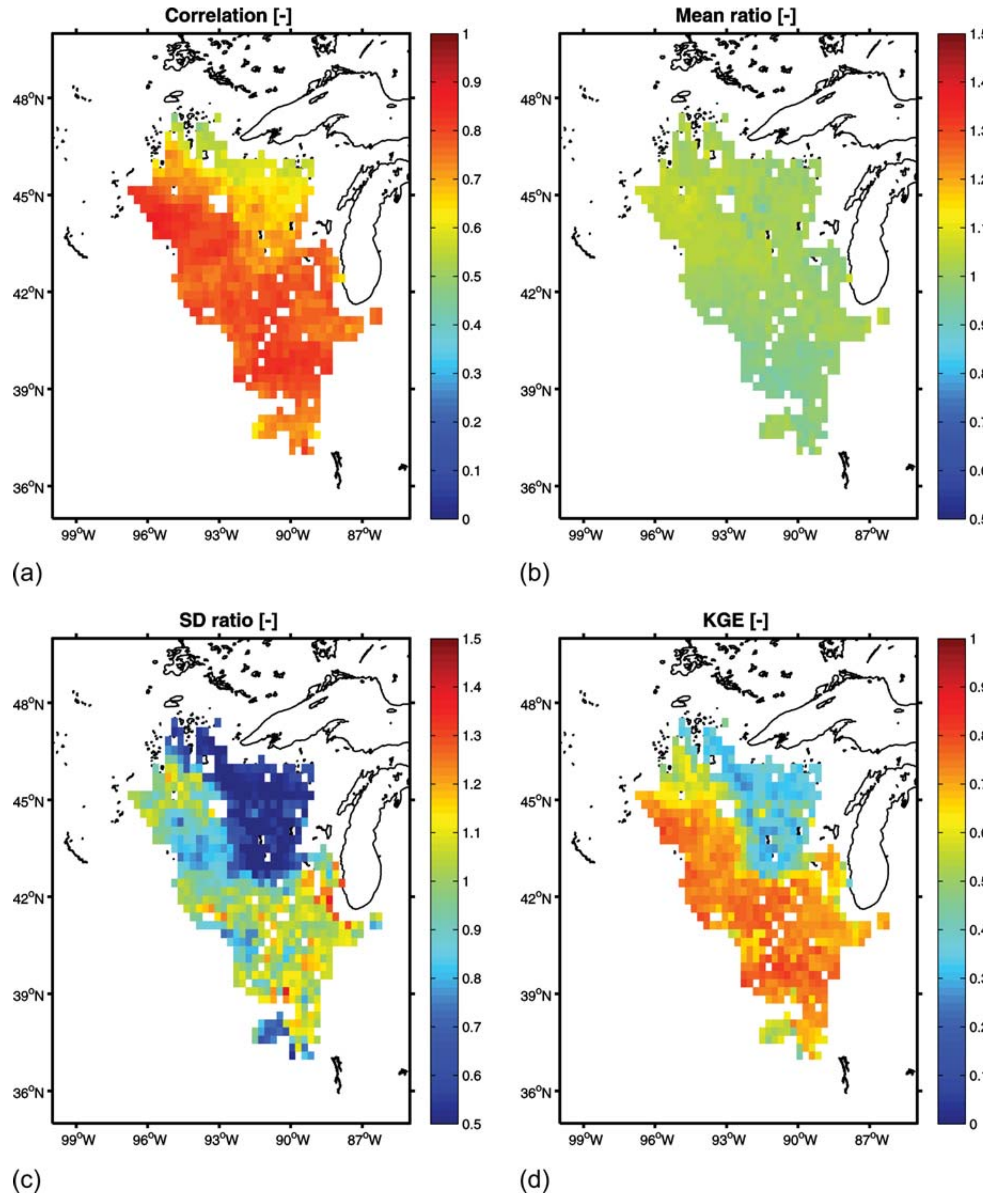

Fig. 10. The 2011 annual mean (a) correlation [−], (b) mean ratio [−], (c) standard deviation ratio [−] and (d) KGE [−] between SMOS TB and simulated TB (case 10) across all incidence angles, polarizations and orbits.

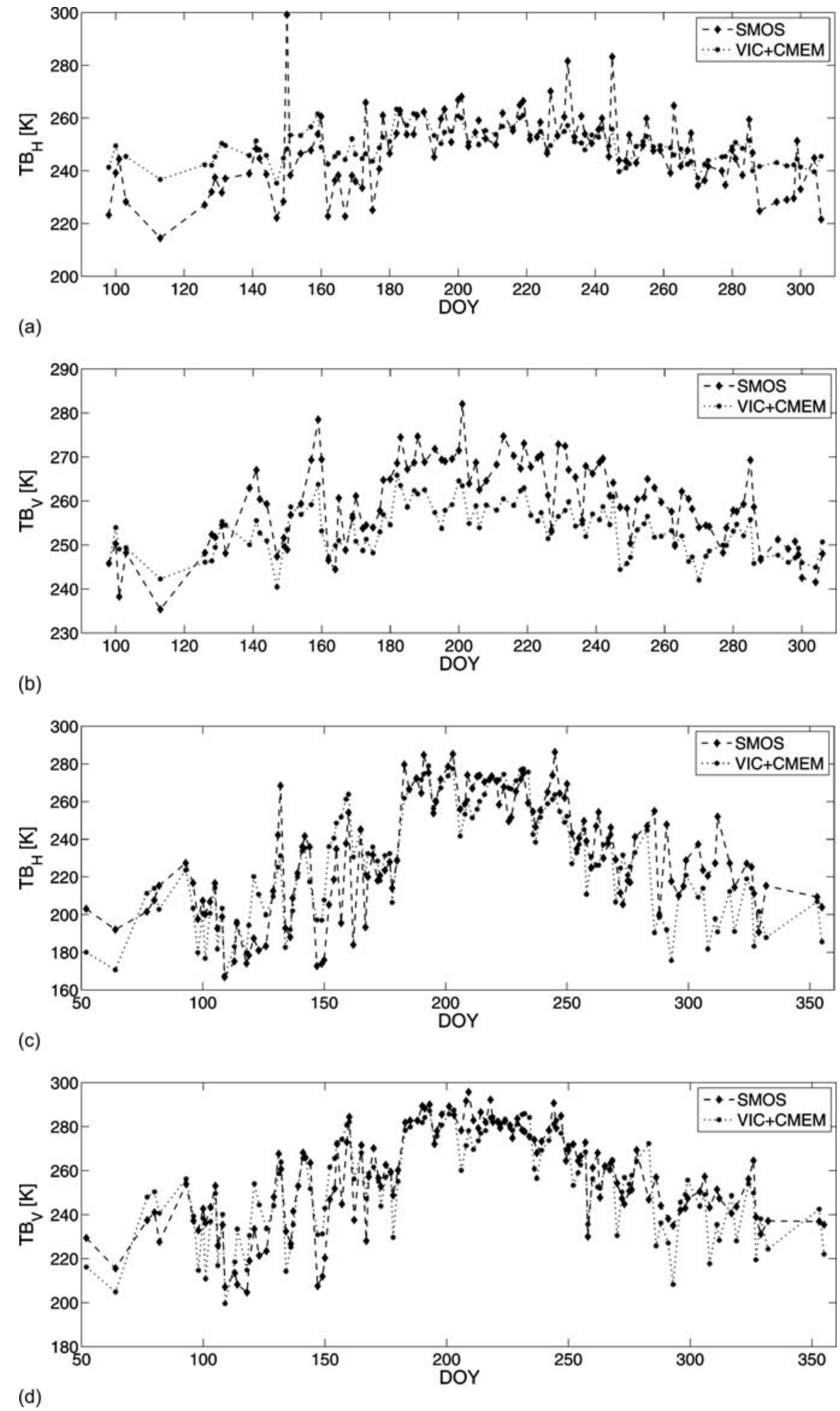

Fig. 11. 2011 time series of ascending TB [K] at 42.5° as observed by SMOS and simulated by VIC+CMEM (case 10), over (a, b) forest and (c, d) cropland grid cells, at (a, c) H-polarization and (b, d) V-polarization.